



Condensin- and Replication-Mediated Bacterial Chromosome Folding and Origin Condensation Revealed by Hi-C and Super-resolution Imaging.

Martial Marbouty, Antoine Le gall, Diego I Cattoni, Axel Cournac, Alan Koh, Jean-Bernard Fiche, Julien Mozziconacci, Heath Murray, Romain Koszul, Marcelo Nollmann, et al.

► To cite this version:

Martial Marbouty, Antoine Le gall, Diego I Cattoni, Axel Cournac, Alan Koh, et al.. Condensin- and Replication-Mediated Bacterial Chromosome Folding and Origin Condensation Revealed by Hi-C and Super-resolution Imaging.. *Molecular Cell*, 2015, 59 (4), pp.588-602. 10.1016/j.molcel.2015.07.020 .
pasteur-01419993

HAL Id: pasteur-01419993

<https://pasteur.hal.science/pasteur-01419993>

Submitted on 5 May 2017

HAL is a multi-disciplinary open access archive for the deposit and dissemination of scientific research documents, whether they are published or not. The documents may come from teaching and research institutions in France or abroad, or from public or private research centers.

L'archive ouverte pluridisciplinaire **HAL**, est destinée au dépôt et à la diffusion de documents scientifiques de niveau recherche, publiés ou non, émanant des établissements d'enseignement et de recherche français ou étrangers, des laboratoires publics ou privés.



Distributed under a Creative Commons Attribution 4.0 International License

Condensin- and replication-mediated dynamic folding of a bacterial chromosome and its origin domain revealed by super-resolution imaging and Hi-C

Martial Marbouty^{*1,2}, Antoine Le Gall^{*3}, Diego I. Cattoni³, Axel Cournac^{1,2}, Alan Koh⁴, Jean-Bernard Fiche³, Julien Mozziconacci⁵, Heath Murray⁴, Romain Koszul^{1,2,#}, Marcelo Nollmann^{3,#}

¹ Institut Pasteur, Department of Genomes and Genetics, Group Spatial Regulation of Genomes, 75015 Paris, France

² CNRS, UMR 3525, 75015 Paris, France

³ Centre de Biochimie Structurale, CNRS UMR5048, INSERM U1054, Université de Montpellier, 29 rue de Navacelles, 34090 Montpellier, France

⁴ Centre for Bacterial Cell Biology, Institute for Cell and Molecular Biosciences, Newcastle University, NE2 4AX, Newcastle Upon Tyne, United Kingdom

⁵ Laboratoire de Physique Théorique de la Matière Condensée, CNRS UMR 7600, Université Pierre et Marie Curie, Sorbonne Universités, 75005 Paris, France

* Co-authors

To whom correspondence should be addressed:

Romain Koszul: romain.koszul@pasteur.fr or

Marcelo Nollmann: marcelo.nollmann@cbs.cnrs.fr

Summary

Chromosomes of a broad range of kingdoms, from bacteria to mammals, are structured by large topological domains, whose precise functional roles and regulatory mechanisms remain elusive. Here, we combine super-resolution microscopies and chromosome-capture technologies to unravel the higher-order organization of the *Bacillus subtilis* chromosome and its dynamic rearrangements during the cell cycle. We decipher the fine 3D architecture of the origin domain, revealing folding motifs regulated by condensin-like complexes. This organization, along with global folding throughout the genome, is present before replication, disrupted by active DNA replication and re-established thereafter. Single-cell analysis revealed a strict correspondence between sub-cellular localization of origin domains and their condensation state. Our results suggest that the precise 3D folding pattern of the origin domain plays a role in the regulation of replication initiation, chromosome organization and DNA segregation.

Keywords: chromosome structure and organization, DNA replication, chromosome segregation, condensins, chromosome conformation capture, super-resolution microscopy, bacterial mitosis.

Introduction

Ensuring the proper propagation of chromosomes over generations is a complex process essential to the survival and evolution of all living organisms. Regulatory mechanisms have evolved to coordinate replication, segregation, and cell division, concomitantly with other DNA-related metabolic processes such as transcription. Within the last 10 years, chromosome capture-conformation (3C) technologies have started to unveil new levels of chromosomal hierarchical organization at the megabase and sub-megabase scales (Dekker et al., 2002). Topological domains (TDs) have originally been defined in higher-eukaryotes as genomic regions within which the chromatin fiber displays a high frequency of preferential contacts (Dixon et al., 2012; Sexton et al., 2012). TD-like domains have been described as well in bacteria where they were defined as chromosomal interaction domains (CIDs) (Le et al., 2013).

A fundamental challenge remains the better understanding of the functional roles of topological domains, in particular how their architecture may affect or be affected by other cellular functions such as DNA replication and segregation. This interplay is especially acute in bacteria, which lack the well-characterized segregation apparatus of eukaryotes. Several mechanisms have been suggested to promote sister segregation, such as passive disentangling thanks to tethering to the cell envelope, active segregation by partition complexes, or mechanical “stress” relief models (Kleckner et al., 2014).

Structural maintenance of chromosome (SMC) are ubiquitous complexes implicated at different hierarchical levels of chromosomal organization as well as in replication and transcription. In eukaryotes, SMC complexes play different roles depending on their protein composition: cohesins are responsible for holding sister chromatids together after replication, whereas condensins ensure faithful segregation through compaction and organization of sister chromatids at the late stages of mitosis (Nasmyth and Haering, 2009). The large majority bacterial clades possess canonical SMC-kleisin-like complexes composed of two SMC subunits, a kleisin (ScpA) and a third factor (ScpB). Most bacteria with SMC-ScpAB complexes also encode a partitioning system with three essential components: a centromere site (*parS*), a centromere-binding protein (ParB), and a Walker-type ATPase (ParA). ParB bound to *parS* recruits SMC-ScpAB complexes to the origin of replication region (Gruber and Errington, 2009; Sullivan et al., 2009) and their

combined action contributes to the resolution of newly replicated origins (Gruber et al., 2014; Wang et al., 2014b). In *Bacillus subtilis* (*B. subtilis*), the chromosome adopts a strict oriC-ter-oriC longitudinal orientation for most of the cell cycle (Berkmen and Grossman, 2006; Wang et al., 2014a). Interestingly, replication origins are located on the nucleoid poles in newborn cells and following replication initiation the duplicated origins are transiently relocalized to the center of the new nucleoids before being actively segregated to opposite positions at the nucleoid edges (Wang et al., 2014a).

Here, we used a unique combination of super-resolution microscopies and chromosome conformation capture (Hi-C) to shed light into the higher-order structure of the *B. subtilis* chromosome and unveil the factors responsible for its regulated folding. This approach revealed the fine 3D architecture of a large domain encompassing the origin of replication, the cycles of origin domain condensation/de-condensation coupled to replication and sub-cellular localization, and the specific roles of the ParABS system, the SMC-ScpAB complex, and active replication in defining global chromosome architecture and origin domain folding.

Results

Higher-order chromosome organization in *B. subtilis*

To investigate chromosome organization in *B. subtilis*, we applied chromosome conformation capture analysis to exponentially growing wild-type (WT) cultures in rapid growth conditions. The resulting contact map (Fig. 1a) shows a strong and broad diagonal reflecting frequent local contacts resulting from interactions among adjacent loci. Several additional notable features emerge upon further analysis.

Three broad global domains. Overall chromosome topology is revealed by converting the contact map into a three-dimensional topological representation (Fig. 1b; (Lesne et al., 2014)). The nucleoid folds into a helicoidal shape, analogous to that also seen in *E. coli* (Fisher et al., 2013; Hadizadeh Yazdi et al., 2012) and *C. crescentus* (Umbarger et al., 2011). Within this folding pattern, three distinct sub-regions (hereafter referred to as "domains") can be discerned, each containing portions of the left and right chromosome arms. First, a large globular region of ~1.4 Mbp encompasses the origin of replication (origin domain, Fig. 1b, box I). This domain is directly visible in the contact map as a region displaying a large number of inter- and intra-arm contacts around *oriC* (Fig. 1a, dashed box). Second, a broad middle region of the genome exhibits very close juxtaposition of the two arms (Fig. 1b, box II). This feature is directly visible in the primary contact map as a distinctive secondary diagonal (perpendicular to the main diagonal, Fig. 1a). Finally, a smaller domain of ~500 kb encompasses the terminus of replication (*ter*) region (Fig. 1b, box III).

Local, short-range domains. An expanded view of the main diagonal of chromosome contacts reveals squares of various sizes (Fig. 1c). This feature implies the presence of local domains that reflect contacts over a range of genomic distances. The smaller domains, defined by contacts at short correlation lengths, were analyzed with respect to size, number and borders using the directionality index (DI) approach (Dixon et al., 2012) (Figs. 1c and S1a). DI analysis reveals the presence of regions in which contacts are absent, i.e. "barriers". Regions between barriers are inferred to define contact subdomains. Over the entire chromosome, we observed 20 statistically-significant barriers, implying the existence of ~20 corresponding interaction domains ranging in size from 50 to 300 kb (mean at 175 ± 50 kb, Fig. S1a). This pattern was not significantly affected

by the genotypes of the strains used (PY79 or BS168A, Fig. S1b). 60 % (12/20) of the barriers coincided with highly-expressed genes. This correlation, previously described in *C. crescentus*, suggests that transcription may hinder interactions of loci that flank the transcribed region (Fig. 1c). However, not all highly-expressed genes generated detectable barriers to interactions. Conversely, a number of regions in the genome generate barriers that do not overlap with transcription hotspots. Interestingly, these regions correspond principally to DNA elements acquired through horizontal transfer that present a low GC% compared to the rest of the genome and are specifically bound by the transcriptional activator Rok (Fig. S1a). Such sequences represented ~30% of the barriers. Short-range interaction patterns were severely disrupted by the treatment of cells with rifampicin, a general transcription inhibitor (Fig. S1b). Irrespective of local influences of transcription, this effect points to an important positive role for transcription in maintenance of global chromosome organization, possibly via its effects on DNA supercoiling (Higgins, 2014).

Organizational and/or temporal complexity in middle-range genomic distances. The primary contact map is unusually complex at middle range genomic distances, with a complicated array of partially overlapping squares (or, in half-contact maps, triangles) (Fig. S1c, triangles). This pattern could result from a tendency for complex, simultaneous contacts comprising “nested” domains with smaller domains interacting with one another and/or embedded within larger domains. Alternatively, it could reflect heterogeneity within the population, with different detailed types of contacts in different cells or at different stages of the cell cycle (e.g. below).

DI analysis provides one description of this complex pattern of domains. This approach directly detects barriers, not domains (above); nonetheless, different combinations of domains with different genomic sizes can lead to the formation of barriers (Fig. S1c, triangles). For the sake of simplicity, and in analogy to domains described in *C. crescentus*, all of the different-sized domains defined by DI barrier analysis will be referred to as ‘chromatin interaction domains’ (CIDs).

Internal architecture of the origin domain

Next, we analyzed the organization of the large origin domain revealed by the contact map and the 3D reconstruction (above). Magnification of the contact map reveals a well-defined substructure comprised of a pair of nested hairpin structures (Figs. 2a). The main hairpin results directly from inter-arm contacts linking the left and right replichores genome-wide (above; Fig. 2a). Importantly, these contacts do not originate at oriC, but rather at a genomic region ~100 kb to the left of oriC. We will refer to this folding motif as the primary hairpin. A second detected signal

suggests the presence of an intra-arm hairpin. This type of motif is manifested in an array of contacts that extend away from the main diagonal as a bow-shaped signal that skews towards the left (away from the origin). The intra-arm hairpin originates at ~-350 kb on the contact map (Fig. 2a). The effect of these hairpins is to bring distant genomic loci on the left replicore into close proximity of oriC. Notably, *parS*³³⁴ is contained within this hairpin and appears to form a sequence-specific loop with a genomic locus located ~125 kb away along the left arm (Figs. 2a-b). The same detailed folding of the origin domain is seen in a variety of growth media (Fig. S1c). These signals suggest an average origin domain organization with two hairpins that regroup several *parS* sites to the vicinity of oriC (diagram, Fig. 2a).

The SMC-ScpAB complex and the ParBS system are implicated in the formation and maintenance of origin domain architecture.

Positioning of *parS* sites, ParB, SMC-ScpAB, and DnaA enrichment sites within the origin domain

To understand the possible factors involved in defining origin domain architecture, we aligned Hi-C contact maps and ChIP protein enrichment profiles for ParB, SMC-ScpAB and DnaA within the origin region (Fig. 2b) (Breier and Grossman, 2007; Gruber and Errington, 2009; Ishikawa et al., 2007). A cluster of three *parS* sites (*parS*^{354,355,356}) is located close to the tip of the primary hairpin, and a strong SMC-ScpAB enrichment is observed at this cluster and at flanking positions (Gruber and Errington, 2009) (Fig. 2b, green arrowheads).

In addition, SMC-ScpAB is enriched at other specific positions. A notable example is provided by a region of sequence-specific contacts between the two sides of the intra-arm hairpin (Fig. 2b, red arrowheads), visualized in the contact map as a dot away from the main diagonal. This specific contact is flanked on one side by *parS*³³⁴, and by a genomic locus located ~125 kb away along the left arm. Interestingly, these two genomic loci are bound by the replicator initiator protein DnaA (Ishikawa et al., 2007) (Fig. 2b). These two distant DnaA boxes are negative regulators of replication initiation (Okumura et al., 2011). Thus, this specific contact and the primary and intra-arm hairpins could serve to bring distant DnaA boxes close to OriC to regulate origin firing (Fig. 2b).

Strikingly and more generally, SMC-ScpAB complexes are enriched at genomic positions displaying symmetrical inter-arm contacts that extend from the *parS*³⁵⁴⁻³⁵⁶ locus to the terminus of

replication (Fig. 2c, red lines). This specific enrichment is consistent with a global, functional "pairing" between arms mediated by SMC-ScpAB.

Taken together, these findings suggest a model in which the origin domain is specifically folded into a nested structure with at least ParB, SMC-ScpAB and DnaA participating in the formation of long-range contacts along entire chromosome arms, local intra-arm contacts within the origin domain, and sequence-specific long-range contacts. A schematic representation synthesizes the folding motifs and contacts described (Fig. 2d).

Absence of *parS*, ParB or SMC-ScpAB results in unfolding of the origin domain.

To determine whether ParABS/SMC-ScpAB are indeed involved in maintaining the organization of the origin domain, we tested the effect of mutants. Strikingly, the contacts resulting from inter- and intra-arm hairpin structures were considerably compromised in the absence of ParB, in a strain without *parS* sites (*parS*-Δ10), or when SMC-ScpAB was depleted, as reflected by the disappearance of perpendicular diagonals at -100 and -350 kb, respectively (Fig. 3a). We noticed that specific contacts within the intra-arm hairpin enriched in DnaA were not perturbed, suggesting that other factors may be implicated in the formation of this folding element. In contrast to wild-type (Fig. 1b), replichore pairing is disrupted in mutant strains as no inter-arm contacts are observed in ParBS/SMC-ScpAB mutants. Loss of pairing is clearly illustrated by three-dimensional topological representations (Fig. 3b). These results are consistent with inter-arm contacts specifically requiring the recruitment of the condensin complex by ParB to the origin region. Thus, the recruitment of SMC-ScpAB to the primary and intra-arm hairpins could drive the overall folding of the chromosome down to the terminus of replication (Fig. 2c).

To directly test at the single-cell level whether ParB-recruited SMC-ScpAB complexes are required to bridge inter-arm contacts, we monitored the distance between two loci within the origin domain in vivo. FROS tags were located close to *parS*³⁵⁹ and *parS*³³⁴, thus marking the opposite sides of the inter-arm contacts detected by Hi-C (Fig. 3c). The distance between FROS tags increased by 75±4 % in the ΔParB mutant with respect to WT (from 100±95 nm in WT to 175±120 nm in ΔParB, mean±s.d.; Fig. 3c). As deletion of ParB decreases proper recruitment of SMC-ScpAB to the origin region (Sullivan et al., 2009), these results are consistent with our proposed role of SMC-ScpAB in mediating inter-arm chromosomal contacts.

Dynamic folding and unfolding of the origin domain in concert with DNA replication.

Next, we investigated whether the features identified above for asynchronous cultures were present at all stages of the cell cycle and/or whether they undergo dynamic changes. We therefore generated contact maps for replication arrested cells (a G1-arrest-like chromosomal state) and throughout their re-start of replication (i.e. release into S phase) using a temperature-sensitive replication initiation mutant (dnaB-ts; Supplemental Experimental Procedures; Fig. S2).

When replication initiation is blocked, the origin domain is largely disorganized: the primary hairpin, and to a lesser extent the intra-arm hairpin, are strongly attenuated (Fig. 3d). Furthermore, this disorganization extended throughout the chromosome, all the way to the terminus region (Fig. S2). These results are consistent with replication-arrested chromosomes following a left-ori/ter-right organization, in agreement with cytological data (Berkmen and Grossman, 2006; Wang et al., 2014a) (Fig. 5g).

Following replication restart, the number of contacts between the two replichores gradually reappear, reaching nearly the original signal observed in asynchronously growing cells after 60 minutes (Fig. 3d). These results demonstrate that a compact, coherent nucleoid organization occurs before and after replication whereas replication per se is accompanied by global disruption of that organization. The signals and processes involved in coupling of these two processes remain to be defined. The most straightforward possibility is that initiation of DNA replication triggers unfolding of the origin domain; however, it remains unclear whether propagation of this disorganization is mediated by the replication process itself or in some other way (see Discussion).

Single-cell super-resolution analysis reveals a new nucleoid substructural feature, the “high-density chromosomal regions” (HDRs).

Chromosome conformation capture typically examines bulk populations of cells. As a complement of Hi-C, we used an original imaging approach to explore the global 3D organization of the bacterial chromosome in single cells. Building upon recent developments (Fisher et al., 2013; Hadizadeh Yazdi et al., 2012), we combined high-density whole-chromosome labelling with high-throughput, three-dimensional structured illumination microscopy (3D-SIM), which provides a

two-fold increase in spatial resolution as compared to previous wide-field epifluorescence studies. Chromosomes were fluorescently-labeled by either chemical staining (DAPI) or by Hbs-GFP, a non-specific DNA binding protein (Smits and Grossman, 2010). Expression of Hbs-GFP does not perturb chromosome architecture (Fig. S2) (Wang et al., 2014a). DAPI is an intercalating dye that could potentially alter nucleoid state. However, we found no significant difference in the patterns given by the two methods (Fig. S3a). Together these approaches provide significantly improved visualization of the 3D organization of nucleoids in living cells (Fig. 4a).

3D-SIM images reveal the existence of high-density chromosomal regions (HDRs) organized along the long axis of the cell (Figs. 4b, S3b-c). HDRs were defined as 3D positions that display convergent, multi-directional gradients of the intensity signal (Fig. 4c and Supplemental Experimental Procedures). HDRs with a size of a single voxel cannot be discerned from camera noise and were discarded. HDRs were not visible in cells in which cytosolic GFP was imaged instead of the nucleoid, implying that they represent true nucleoid signals rather than imaging noise (Fig. S3c-d). Time-lapse analysis shows that HDRs are relatively stable structures over periods of tens of seconds (Fig. S3d). By performing high-throughput super-resolution microscopy on thousands of cells, we obtained statistically significant distributions of the number and cellular localization of HDRs.

For a population of slowly growing cells in exponential phase, the average number of HDRs in newborn nucleoids was 7.9 ± 2.1 (mean \pm std) (Figs. 4d, left panel, and S5a). In replication-arrested cells, the average number of HDRs was 8.5 ± 2.2 (mean \pm std) (Figs. 4d, middle panel, S5a). After release of the replication block, the number of HDRs increases linearly with nucleoid length, rising to 15 ± 4 HDRs (mean \pm std) detected before cell division as expected for a doubling of genome content (G1+50min; Fig. 4d, right panel). The mean number of HDRs detected for nucleoids in newborn cells also increases from minimal to rich media (Fig. S4a), again consistent with a higher chromosome copy number in faster growth rate conditions. These results reveal the existence of a new level of chromosomal sub-organization, made possible by the gain in spatial resolution afforded by 3D-SIM (Fig. S3b).

To further quantify these structures, we estimated the average percentage of DNA per HDR from the cumulative fluorescence signal within each HDR and the total nucleoid signal in G1 arrested cells (Fig. 4e). As these cells contain a single chromosome, we estimated semi-quantitatively a reference mean amount of DNA per HDR (~230 kb). Interestingly, the distribution

of the percentage of DNA within HDRs in exponentially growing cells for nucleoids of comparable sizes (WT; Fig. 4e, green curve) was similar to the distribution in G1, consistent with the mean size of HDRs being conserved between these two states.

The existence of a higher-order nucleoid sub-organization has not previously been reported. It is thus of interest to know whether/how HDRs are related to genomically-specified organizational features. CIDs comprise DNA domains presenting enriched contacts and are thus expected to be present in condensed regions within the cell. However, HDRs are substantially larger than the average CID as defined above. We therefore imagine that HDRs might arise as a physically-based organizational feature that, in addition, may often represent stochastic groupings of CIDs. Preliminary experiments measuring the co-localization of fluorescent repressor operator arrays (FROS) tags within CIDs and HDRs (Fig. S4b) are consistent with this hypothesis which, however, requires extensive further consideration.

We used the new perspective provided by 3D-SIM analyses to further explore the influence of ParABS/SMC-ScpAB and DNA replication on chromosome structure and dynamics. Different parameters were analyzed in WT cells or in cells depleted for SMC-ScpAB, deleted for the parB gene (Δ ParB), or arrested in G1 (Fig. 4f). Analysis of asynchronous cultures revealed that nucleoid lengths and widths vary little upon SMC-ScpAB depletion (Figs. 4g-h). For Δ ParB, width and lengths were considerably larger, consistent with the increased activation of replication origins, and thus genomic content, observed in this mutant (Okumura et al., 2011). Replication-arrested cells displayed similar widths but considerably shorter lengths than asynchronous cells (Figs. 4g-h), consistent with the presence of a single chromosome.

Interestingly, HDRs existed in all conditions, irrespective of the organization suggested by Hi-C. The mean radial distance of HDRs away from the longitudinal nucleoid axis increased for replication-arrested cells and Δ ParB/SMC-ScpAB mutants (Fig. 4i). Finally, the mean HDR density, defined as the total number of HDRs over the nucleoid volume, remained unchanged in WT cells but increased considerably in absence of ParB or SMC-ScpAB (Figs. 4j-k). Representative nucleoids and schematic representations of the effects of mutations are summarized in Fig. 4l. Overall, these data indicate that the number of HDR per genome equivalent is relatively constant throughout the cell cycle, despite global changes in nucleoid shape over time. The increased numbers and dispersion of HDRs in mutants compared to wild-type possibly reflect a more open conformation of the replichores, consistent with Hi-C data in G1-arrested cells.

The origin of replication is contained within a single prominent HDR that persists throughout the cell cycle.

The Hi-C results presented above point to the existence of a large folded origin domain present in G1 that unfolds during S-phase and reappears after replication. We next investigated whether the origin domain might correspond to an HDR and, more generally, whether HDRs displayed a conserved sub-cellular localization throughout the cell cycle and between cells. Direct averaging of 3D images of nucleoids of similar sizes lead to a blurring of HDR positions resulting in the loss of structural information (Fig. S5a). To overcome this averaging effect, we determined the positions of each HDR in nucleoids along the longitudinal and radial axes. We then computed, for nucleoids of the same size, the (2D) histogram of HDR positions along these two axes (Fig. S5a, Supplemental Experimental Procedures). This procedure yielded robust, characteristic patterns of HDR localization with only a few hundreds of cells (Fig. 5a). Despite the presence of ~5-15 HDRs in each cell, only a small number of maxima are observed in the histograms of HDR positions. These maxima represent positions where an HDR occurs with high probability, thus identifying the specific cellular positions where HDRs are more likely to be observed.

HDR positional distributions determined in an asynchronous population were used to evaluate dynamic changes in positional preferences over time in the cell cycle, using increasing nucleoid length as a time metric. This information is displayed, for a given population, as a 2.5D kymograph-like representation (Figs. 5b, and S5b). In a WT culture growing under slow growth conditions, HDR maxima display a well-defined choreography (Fig. 5b, left). The smallest cells exhibit a single prominent local maximum of HDR probability at the center of the nucleoid (darkest red signal in the kymograph and black signal in 2D histograms). As nucleoid size begins to increase, this single HDR maximum splits in two maxima that migrate towards the poles, where they remain for most of the cycle. At a later stage, the two HDR maxima relocate to the centers of two new discrete nucleoids. Finally, after sister nucleoids split, these maxima migrate to their starting positions at their respective new poles.

The pattern of segregation observed for this maximum HDR density signal corresponds to that expected for the dynamic positioning of the origin region as defined by previous FROS studies

(Berkmen and Grossman, 2007; Wang et al., 2014a). Thus, we refer to this maxima as origin-correlated HDR (ori-HDR). This correlation was directly documented by five further analyses.

First, the segregation pattern of ori-HDRs corresponds to a large degree to that of ParB-GFP (Figs. 5c and S5b-c), which is known to bind over the entire origin domain and is normally used as a marker of the oriC position (Sullivan et al., 2009).

Second, we analogously analyzed the positioning of an origin-proximal FROS tag (at 359° on the genome map) and of ParB-GFP in a strain carrying only a single, unique *parS* site at the corresponding position. In both cases, the segregation pattern (blue – red color-scale) closely resembles the trajectory of ori-HDR (Fig. 5d, dotted lines). FROS tags in other positions (174°, 240° and 273°) exhibit very different segregation patterns (Fig. 5e).

Third, we directly visualized HDRs and ParB-GFP simultaneously in a strain containing a single *parS* site close to the origin of replication (*parS*³⁵⁹; Fig. 5f, left panel). A striking correlation can be observed between the localization of ori-HDR (represented by the z-axis of the distribution) and ParB-GFP signal (color-scale superimposed to the HDR pattern; Figs. 5f, right panel, and S5c).

Forth, as expected from FROS analysis (Wang et al., 2014a) and Hi-C analysis (above), G1-arrested cells displayed a unique HDR maximum at the center of the nucleoid (Fig. 5g, left panel). After replication re-start, two HDR maxima predominantly relocalized to the edges of the nucleoid (Fig. 5g, right panel), following the re-localization pattern of origins after replication re-start (Wang et al., 2014a).

Fifth, depletion of SMC-ScpAB or deletion of *parB*, both of which result in disorganization of the origin domain, lead to somewhat aberrant segregation patterns of ori-HDRs (Fig. S5c).

Taken together, these results strongly suggest that oriC is part of a discrete and dense structure that persists throughout the cell cycle.

Super-resolution analysis of origin domain states

Since *parS* sequences are distributed throughout the origin domain defined by Hi-C, super-resolution visualization of *parS*-bound ParB-GFP provides a proxy to the spatiotemporal dynamics of this domain from a perspective complementary to that of Hi-C (Fig. 6a, inset).

3D-SIM and 3D-PALM imaging showed that several discrete ParB-GFP sub-clusters group together in a larger ParB cluster in slowly-growing, asynchronous WT cells (Fig. 6a). The sub-

cellular localization and segregation pattern of ParB clusters corresponded to that of *oriC* (compare Figs. 5c and 5d). Thus, each ParB-GFP cluster represents a single origin domain (Fig. 6a). ParB-GFP sub-clusters were individually detected and grouped together to determine the number of sub-clusters forming each ParB cluster (Fig. S6a). The mean number of ParB-GFP sub-clusters per ParB cluster was 2.8 ± 2 (mean \pm s.d) (Fig. S6b). To validate this approach, we determined the ParB-GFP distribution in a strain carrying only a single *parS* site at the origin (*parS*³⁵⁹, strain *parS*- $\Delta 7$). In this case, ParB clusters containing a single (1.2 ± 0.8 , mean \pm s.d), isolated ParB-GFP sub-cluster were visualized (Figs. 6b, S6b). These single ParB sub-clusters predominantly localized at nucleoid edges (Fig. 5f). The size of ParB-GFP clusters in *parS*- $\Delta 7$ corresponded to the resolution limit (Fig. S6a). Thus, ParB-GFP clusters in WT cells represent combinations of *parS* sites that group together to form an origin domain.

The validity of this assumption was further confirmed by computing the average number and relative distance between ParB clusters. In both WT and *parS*- $\Delta 7$, the number of ParB clusters per nucleoid (1.9 ± 0.6 for WT and 2.0 ± 0.7 for *parS*- $\Delta 7$, mean \pm s.d) and the average maximal distance between ParB clusters (1500 ± 450 nm for WT and 1400 ± 500 nm for *parS*- $\Delta 7$, mean \pm s.d.) were consistent with two origin domains located at the edges of the nucleoid in most cells (Figs. 5c, S6b) (Berkmen and Grossman, 2007; Wang et al., 2014a).

The size of origin domains in WT cells was then estimated from the distances between the most widely separated ParB-GFP sub-clusters within single ParB clusters. Domain sizes were widely distributed, with an average size of 440 ± 210 nm (mean \pm s.d) (Fig. S6c). ParB cluster sizes were slightly smaller when measured using 3D-PALM due to the higher resolution of this method, cell fixation, and differences in the clustering algorithms used (Fig. S6c). Importantly, both estimations were consistent with our previous measurements using FROS tags (Fig. 3d). These results suggest that the origin domain is composed of several independent *parS* sites with distinct, resolvable physical positions that likely corresponds to the positions of *parS* sites/interactions suggested by Hi-C analysis (Fig. 2c).

Next, analysis of the distribution of ParB-GFP cluster sizes and compositions was used to probe for changes in the state of the origin domain during cell cycle progression. We measured the changes in the number of ParB sub-clusters per ParB cluster and the sizes of ParB clusters as a function of nucleoid size and sub-nuclear localization (Figs. 6c-d, and S6c). ParB-GFP cluster density was plotted as a function of nucleoid size and axial positions, resulting in the same type of

2.5D kymograph representation as described above. The colorscale of this density pattern reflects variations in either the number of ParB sub-clusters per ParB cluster, or in ParB cluster sizes (Figs. 6c-d, and S6c). Strikingly, origin domains were highly condensed while positioned at the nucleoid edges as revealed by the small size and small number of sub-clusters, but displayed a large increase in the number of sub-clusters and size as they approached the centers of new nucleoids (Fig. 6c-d). A similar trend was observed for *parS-Δ7* cells, although these cells displayed considerably lower number of sub-clusters and sizes (Fig. 6e-f).

Overall, this pattern of condensation and decondensation of the origin domain corresponds closely to the program of replication-correlated unfolding and refolding of the origin domain defined by Hi-C (Fig. 2), and that displayed by ori-HDR (Fig. 5), suggesting that condensin loading at the origin following replication may participate in the refolding of the origin domain.

Discussion

In this work, we combined Hi-C and super-resolution microscopies to reveal and dissect several important mechanisms and functions of chromosome folding within a model bacterium.

Chromosomal interaction domains in *B. subtilis*

Previous Hi-C studies on *C. crescentus* proposed that barriers between CIDs domains are mainly due to highly-transcribed genes blocking the diffusion of free supercoils (Le et al., 2013). This model is consistent with studies in *E. coli* and *Salmonella enterica* showing that transcription activity from strong promoters promotes the formation of topological barriers (Booker et al., 2010; Higgins, 2014). In these species, however, topological barriers were observed at considerably shorter length-scales (~10-15 kb) (Postow et al., 2004), with only very highly transcribed genes (e.g. *rrn* genes) accounting for ~8% of the detected topological barriers (Booker et al., 2010). Our Hi-C analysis shows that a large proportion of transcription hotspots in the *B. subtilis* chromosome fail to produce barriers between CIDs. Conversely, a considerable number of barriers fail to correlate with regions of high transcriptional activity, but instead overlap with the genomic positions of a nucleoid-associated protein (Rok) (Smits and Grossman, 2010), and of AT-rich sequences acquired through horizontal gene transfer. This specific enrichment of mobile genetic elements at barriers indicates that these genetic loci may be particularly susceptible or permissive to rearrangement events, possibly due to the pause or collapse of replication forks. This enrichment was also observed in higher eukaryotes (Sexton et al., 2012). Overall, these observations are consistent with several functional activities- besides transcription- playing a role at establishing barriers between CIDs.

HDRs represent a new organizational feature of the chromosome

Using 3D-SIM combined with whole-chromosome labeling, we discovered a level of chromosome organization (HDRs) that is not visible by diffraction-limited fluorescence microscopy methods (Fisher et al., 2013; Hadizadeh Yazdi et al., 2012; Le et al., 2013). HDRs are substantially larger than the average CID, suggesting that HDRs may often represent stochastic associations of

CIDs. FROS tags within CIDs were found to often localize within HDRs, consistent with this hypothesis. Further experiments, however, are needed to establish the specific genomic nature of HDRs. The spatial modulation of chromosome density within HDRs is a key feature that may need to be taken into account to model the physical state of the chromosome. HDRs exist in all cells, but only ori-HDRs display a conserved sub-cellular localization with a well-defined cell-cycle choreography. This observation suggests that the sub-cellular localization of ori-HDR may be specifically regulated, possibly to control replication state and to propagate specific folding patterns from the origin towards the remainder of the chromosome. Further experiments in other species will be required to determine whether HDRs are a universal feature of bacterial chromosomes.

Organization and potential function of the origin domain

In *B. subtilis*, replication origins localize to the edge of the nucleoid for most of the cell cycle (Fig. 5) (Berkmen and Grossman, 2006; Wang et al., 2014a), where they appear highly condensed (Fig. 6). Thus, the specific folding pattern captured by Hi-C technologies from an asynchronous population (Fig. 2) reflects primarily the structure of origins at this sub-cellular position (Fig. 7a). Interestingly, DnaA binds not only to boxes in the oriC-proximal region, but also to six other distant boxes located in intergenic regions (Ishikawa et al., 2007) (Fig. 2b). Despite their distance to the origin, intergenic DnaA boxes act to inhibit replication initiation (Okumura et al., 2011; Smits et al., 2011). Our results suggest that the origin domain folding brings distant DnaA boxes in the vicinity of oriC (Figs. 2d and 7a), suggesting that origin domain architecture may play a role in the regulation/inhibition of replication initiation.

Dynamics of origin domain folding during the cell cycle

The widths and shapes of the primary and intra-arm hairpins suggest that the origin domain has a dynamic and/or heterogeneous architecture (Fig. 2a). Our single-cell super-resolution measurements revealed size variations that occur concomitantly with sub-cellular repositioning during the cell cycle (Figs. 5 and 6). Recently, Wang et al. suggested that origins are replicated at the nucleoid edges before being repositioned to the middle of new nucleoids where they embark upon bi-directional segregation (Wang et al., 2014a). Origin re-localization seems to be correlated with a re-organization of the chromosome from a longitudinal to a transverse orientation (Wang et

al., 2014a). Our microscopy data shows that origin domains remain condensed at the nucleoid edges, with origin de-compaction occurring specifically at the middle of new nucleoids (Fig. 6). This origin re-localization may be accompanied by a general reorganization of the origin domain in which inter-arm replichore contacts are disrupted to establish a G1-arrest-like configuration (Fig. 7b). The signals and processes coupling changes in origin domain structure to origin firing remain to be elucidated. The most straightforward possibility is that initiation of DNA replication may trigger the unfolding of the origin domain coupled to dissociation of ParB/SMC-ScpAB. Alternatively, unidentified factors/processes may initiate origin firing, triggering the ensuing structural re-organization and re-localization of the origin region.

After reaching their new mid-nucleoid positions, origin domains may promptly re-establish their original folding by pairing replichores together through SMC-ScpAB-mediated intra- and inter-arm contacts (Fig. 7c). The establishment of this condensed origin structure requires the ParBS partition system, the SMC-ScpAB complex, and active replication (Figs. 3 and 5), supporting the role of condensin complexes in the resolution of newly replicated origins (Gruber et al., 2014; Wang et al., 2014b). Replichore re-zipping is presumably initiated from the cluster of *parS* sites (*parS*^{354,355,356}) (Figs. 2 and 3), consistent with similar observations in *C. crescentus* (Umbarger et al., 2011). The refolding of the origin domain after replication could thus serve to inhibit replication initiation until the next cell cycle. Consistently, deletion of *parB* and *DnaA* boxes lead to severe chromosome segregation defects that can be suppressed by mutations in a replicator inhibitor (*ParA*) (Okumura et al., 2011). In addition, fast and ordered refolding of newly replicated origins may optimize their resolution by limiting DNA catenation between sister chromatids (Gruber et al., 2014). Finally, origin refolding would allow the ParABS partition machinery to recognize pairs of replicated origins for segregation into different directions, mirroring the role of eukaryotic centromeres in allowing the spindle to recognize pairs of replicated products during mitosis.

Roles of SMC-ScpAB in chromosome pairing

Inter-arm pairing is first established at the newly replicated origins but gradually extends to the remainder of the chromosome with the progression of replication (Fig. 3). SMC-ScpAB complexes are recruited to the origin region by specific contacts with ParB (Gruber and Errington, 2009; Sullivan et al., 2009), but may subsequently shift from *parS* sites to promote long-range contacts along the entire replichores (Figs. 1b, 2c). Overall, these observations are consistent with

a model in which SMC-ScpAB complexes: (1) are recruited to the origin region where they convert to a topologically-closed ring encompassing two or more double-stranded DNA segments (Soh et al., 2015); (2) diffuse/slide away from the recruitment site in a closed ring conformation, maintaining cohesion between replichores; (3) break open in a stochastic or regulated fashion, probably requiring nucleotide hydrolysis. This model is consistent with two populations of SMC-ScpAB coexisting in the cell: a static population at the origin, and a highly-mobile population that appears to scan the nucleoid (Kleine Borgmann et al., 2013). The concomitant spreading of replichore pairing with replication may occur in a regular or discontinuous manner, and may help in condensation of the two newly replicated chromosomes to facilitate segregation (Gruber et al., 2014; Wang et al., 2014b). The re-establishment of a precise and ordered longitudinal choreography may be essential to promptly act upon external stimuli to induce developmental changes (e.g. *oriC*-tethering to cell pole early in sporulation) and to reinitiate normal chromosome choreography during spore germination.

Despite the apparent simplicity of bacterial chromosomes and their lack of constitutive chromatin, several fundamental principles of eukaryotic higher-order DNA organization are present in this kingdom. It is tempting to hypothesize that the mechanism of recruitment and spread of SMC-ScpAB, as well as the role of ParABS, may be paralleled to the mechanisms employed by condensins/cohesins and chromatin insulators in eukaryotes. Excitingly, our results represent a striking example of how the 3D folding dynamics of the chromosome fiber itself may be functionally coupled to other DNA management processes and involved in its own regulation.

Experimental Procedures

General Methods

B. subtilis strains were derived either from the prototrophic strains PY79 or BS168. The strains used are listed in Table S1. The construction of plasmids is described in the Supplemental Experimental Procedures and Table S2. Cells were grown in minimal and rich media at 30 °C. Cell synchronizations were performed as previously described with minor changes. Refer to Supplemental Experimental Procedures for more details.

3D-SIM and 3D-PALM

3D-SIM imaging was performed on an OMX V3 microscope (Applied Precision Inc) as previously described (Fiche et al., 2013). Reconstruction and alignment of 3D-SIM images was performed using softWoRx v 5.0 (Applied Precision Inc). 3D-PALM imaging was performed as described previously (Cattoni et al., 2013; Fiche et al., 2013). For 3D-PALM, a MicAO 3D-SR module (Imagine Optic™, France) was used. Refer to Supplemental Experimental Procedures for more details.

Hi-C

Chromosome conformation capture experiments were performed as described elsewhere (Marbouty et al., 2014). Sequencing data were processed into genome-wide contact maps (4 kb bins) that were normalized using the sequential component normalization procedure described previously (Marbouty et al., 2014). Raw contact maps are available on the Sequence Read Archive (SRA) under bioproject-ID PRJNA289589 biosample-ID SAMN03856048. Full details are provided in Supplemental Experimental Procedures.

Author Contributions

Investigation, A.L.G., D.I.C., M.M., J-B.F.; Data Curation, A.L.G, M.N., and A.C.; Formal Analysis, A.L.G., M.N., R.K., A.C., J-B.F., M.M. and J.M.; Software, A.L.G, M.N., J-B.F., and J.M.; Methodology, A.L.G., D.I.C., M.N., J-B.F., and R.K.; Conceptualization, M.N., R.K., A.L.G, D.I.C; Writing – Original Draft, M.N., R.K., A.L.G., D.I.C.; Writing – Review & Editing, M.N. and R.K.; Funding Acquisition, M.N., H.M., and R.K.; Resources, A.K., H.M., and J.M.; Supervision, M.N. and R.K.

Acknowledgements

We thank J. Bonnet and O. Espeli for critical reading of the manuscript, Marie Schaeffer for her ideas on data interpretation, A. Rappailles for help in preparation of initial 3C/Hi-C libraries, and A. Grossman and D. Rudner for sharing strains. Research was supported by European Research Council Starting Grants to R.K. (ERC-Stg-260822) and M.N. (ERC-Stg-260787), and by a Royal Society University Research Fellowship and a BBSRC Research Grant (BB/K017527/1) to H.M. M.M. is the recipient of a fellowship from the Association pour la Recherche sur le Cancer (20100600373). 3D-SIM experiments were performed at Montpellier RIO imaging. We acknowledge support from France-Biolmaging (FBI, ANR-10-INSB-04), and Imagine Optic.

Figure legends

Figure 1. Whole chromosome organization in *B. subtilis*

(a) Normalized genomic contact map obtained from an asynchronous population (rich medium). X and y-axis represent genomic coordinates centered at *oriC* (pink circle). Left and right arms are represented by red-yellow and blue-green gradients. Black arrows outline features of interest described in panels b, c and Fig. S1c. White dashed box represents the origin domain as defined in panel b. The color scale reflects the frequency of contacts between two regions of the genome (a.u.), from blue (rare contacts) to red (frequent contacts), and is conserved across all panels of all figures to facilitate reading. Strain: HM1320.

(b) 3D representation of the contact map from panel a. The chromosome is represented as a chain of beads (1 bead = 4 kb, see Supplemental Experimental Procedures). Beads color-code reflects linear genomic position along the chromosome (same as in panel a). Dotted squares highlight broad global domains (see text). See also Supplementary Movie 1.

(c) Top panel: magnification of contacts within a 250 kb window of the right chromosomal arm. Middle panel: DI analysis of the corresponding genomic region. Downstream (red) and upstream bias (green) are indicated. CIDs are represented as grey triangles. Lower panel: transcription signal (Nicolas et al., 2012). Genomic annotations of highly expressed genes (light blue rectangles), horizontal gene transfer elements (yellow rectangles), and rRNA genes (purple asterisks) are indicated. Blue, yellow and purple vertical lines represent barriers between domains coinciding with these elements. See also Figs. S1a, c.

Figure 2. Structural organization of the origin domain

(a) (i) Magnification of the normalized genomic contact matrix from Fig. 1a encompassing a ~2,000 kb region around *oriC*. Yellow solid line indicates the position of the origin. Positions of *parS* sites are indicated as cyan boxes and lines. Secondary diagonal and bow-shaped structures passing through -100 and -350 kb, respectively are indicated by blue and green dotted lines, while the coordinates at which they cross the main diagonal are shown by white dotted lines. (ii) (left) 3D representation of the origin domain, and (right) schematic representation of the main elements in

the contact map. (iii) Schematic representation of the putative folding of part of the origin domain. Strain: HM1320.

(b) Contact map from 1200 kb to *oriC*. *ParS* sites positions are indicated as cyan solid lines throughout. ChIP-chip enrichment profiles for SMC-ScpAB, DnaA, and ParB are displayed under the contact map (red, pink, blue, respectively). Red arrowheads and lines highlight the enrichment of SMC-ScpAB, DnaA and ParB on the specific contact made by *parS*³³⁴. Green arrowheads indicate peaks of SMC-ScpAB in the vicinity of *oriC*. Blue arrowheads indicate peaks of SMC-ScpAB far from *oriC*. Strain: HM1320.

(c) Circos plot representation of genome-wide contacts and the ChIP profile of SMC-ScpAB (Supplemental Experimental Procedures). Outer ring: chromosome coordinates (kb). Inner blue profile: SMC-ScpAB enrichment. Only inter-arm contacts (secondary diagonal) were used. Light grey lines: subset of inter-arm contacts randomly selected. Red lines: contacts between two genomic sites enriched in SMC-ScpAB. Black lines: contacts between one region enriched in SMC-ScpAB and a non-enriched region. Strain: HM1320.

(d) Schematic representation of the putative average structure of the origin domain. Right and left replichores are represented in blue and red, respectively, with pink and yellow circles representing *oriC* and *dnaA* boxes. *ParB/parS* complexes are shown as orange hexagons with their chromosomal positions displayed in degrees. SMC-ScpAB complexes are represented as blue/green tweezers.

Figure 3. Roles of ParBS, SMC-ScpAB and replication in chromosome organization.

(a) Magnification of the normalized contact maps for SMC-ScpAB-depleted cells, Δ *parB*, and Δ *parS* mutants (see Fig. S2 for full contact maps). Color-codes for chromosome representations (top) and contact frequencies were as in Fig. 1a. Red triangles indicate the positions of *parS* sites. Solid yellow lines indicate the position of *oriC*. Strains: AK487, AK525 and AK215.

(b) Two views of a three-dimensional representation of the contact map of SMC-ScpAB-depleted cells. The chromosome is represented as in Fig. 1b. See also Supplementary Movie 2. Strain AK487.

(c) Left panels: Effect of *ParB* in origin domain folding was determined in live cells by measuring the distance between two FROS tags positioned at 359° and 334° (FROS-1 and FROS-2, green and red stars respectively) in WT and Δ *parB* cells. Right panel: Distribution of distances between FROS-1 and FROS-2 for WT and Δ *ParB* strains (blue and red dots, respectively). Black solid lines

represent a fit to a log-normal distribution. Inset: representative microscopy image of a field of cells (bright field) superimposed with the fluorescence signals of FROS tags (green and red, respectively). Strains: AK359 and HM923.

(d) Magnification of normalized contact maps for *dnaB-ts* cells arrested in G1 (left) and released into S-phase after 5 (middle), and 60 (right) minutes (Fig. S2 for full contact maps). Red triangles indicate positions of *parS* sites and red dotted line indicates the position of the two the secondary diagonal and the bow-shaped structure at -100 and -350 kb, respectively. Solid yellow lines indicate the *oriC* position in the contact maps. Strain: HM890.

Figure 4. High-density chromosomal regions (HDRs).

(a) 3D-SIM volume of a DAPI-stained nucleoid. Light gray to red color-scale represents low to high DNA intensities, respectively. Dotted square highlights the magnified region shown in panel c. Scale bar: 500 nm. Strain: PY79. See also Fig. S3a.

(b) Left panel: schematic representation of the upper resolution limits of conventional and 3D-SIM microscopies in Fourier space (solid blue and green dashed circles, respectively). Middle plane of a DAPI -stained nucleoid band-passed filtered using a 3D butterworth low-frequency filter with a spatial cutoff at 200 nm (middle panel), and a band-pass filter with spatial cutoffs at 100 and 400 nm (right panel). Scale bar: 500 nm. Strain: PY79. See also Fig. S3b.

(c) Higher DNA density region from the nucleoid in panel a (dotted square). Black arrows in middle panel represent the directions of the gradient in intensity signal at the position of a local maximum. This local intensity maximum (green sphere in bottom panel) corresponds to an HDR. See also Fig. S3c.

(d) 2D kernel density plots of the number of HDRs vs. nucleoid length. Left panel: asynchronously growing cells in minimal media. Middle panel: G1-arrested cells. Right panel: cells 50 min after replication block release. N: number of nucleoids analyzed. Strains: PY79 and HM890. See also Fig. S5a.

(e) Estimation of HDRs DNA content in WT and G1-arrested cells for nucleoids of lengths between 1200 and 1400 nm (green and red lines, respectively). The upper x-axis describes HDR genomic size estimated from G1-arrested cells (containing a single chromosome) where the genomic content of the full nucleoid is known.

(f) Schematic representation of a single nucleoid (grey cylinder) and automatically-detected HDRs represented as colored spheres. The radial distance between the detected HDRs and the nucleoid long axis is indicated by a red arrow.

(g,h) Kernel density distributions of nucleoids length (g) and width (h) for two asynchronously growing WT strains (wt1, wt2), SMC-ScpAB-depleted (SMC-depl), Δ ParB cells (Δ ParB) and synchronized G1-arrested cells. Strains: PY79 (wt1), HM1320, HM671 (wt2), AK488, AK525.

(i) Boxplot of HDR radial distances normalized by nucleoid width for the same cell lines depicted in panels g and h. Box represents the first and third interquartiles, horizontal bar within the box represents the median, and the errorbars represent minimum and maximum of distribution. Radial distances were computed as the mean of a running average (window of 200 nm and step size of 200 nm) of the radial distances of HDRs in nucleoids of lengths comprised between 1200 and 2000 nm.

(j) Mean number of HDRs per nucleoid as a function of the nucleoid volume in wild type cells (wt1, PY79, dark green solid line) and SMC-ScpAB depleted cells (SMC-depl., AK488, dark blue solid line). Nucleoid volumes were computed by summing the number of voxels in each individual nucleoid multiplied by the volume of a voxel (voxel = $2.10^{-4} \mu\text{m}^3$). Blue and green shaded areas represent the standard deviation in the number of detected HDRs per nucleoid volume.

(k) HDR density (in number of HDRs per μm^3) for the same cell lines as in panels g and h. HDR density was estimated as the slope from a linear regression of the total number of detected HDRs per nucleoid as a function of nucleoid volume (see panel j). See panel (i) for explanation of boxplot.

(l) Top: schematic representations (similar to the one depicted in panel f) of nucleoids and HDRs spatial distributions for the different cell lines used in panels g-k. Bottom: corresponding 3D images (similar to the one presented in panel a) of representative nucleoids for each strain.

Figure 5. The spatial organization of the nucleoid: heterogeneity of HDR distributions

(a) Scheme depicting the procedure for constructing the 2D probability density histograms of HDR positions within nucleoids. HDRs coordinates were normalized with respect to each nucleoid and then integrated with HDRs coordinates from nucleoids of same length. N: number of nucleoids analyzed for each 2D histogram. See Supplemental Experimental Procedures and Fig. S5a.

(b) 2.5D kymograph of HDRs localization in DAPI-labeled nucleoids. Axes represent the axial position of HDRs and the nucleoid sizes. Both color map and z-axis (i.e. topography) represent HDRs localization density. Right panel: 2D density histograms of HDRs for varying nucleoid

lengths extracted from the kymograph. N: number of nucleoids analyzed. Strain: PY79. See also Figs. S5b-c.

(c) 2.5D kymograph of ParB-GFP localization as a function of their axial position and nucleoid length. The kymograph were generated using the same algorithm described in panel b, but including all ParB-GFP clusters independently of their radial distances. Right panel: 2D density histograms of ParB-GFP detected in DAPI-labeled nucleoids for varying nucleoids lengths extracted from the kymograph. N: number of nucleoids analyzed. Strain: HM671.

(d,e) Cell cycle localization kymographs of FROS tags. (d): labelling of the *oriC* region in cells harboring either all *parS* sites (origin FROS in WT) or containing a single *parS* site near the origin (ParB-GFP in *parSΔ7*). (e): labeling of genomic positions located at the *ter* (Terminus-FROS in WT), at one-third of left arm (Mid-arm FROS in WT) and at a mid-position along the left arm (Mid-arm FROS in WT). Schematic representations of the chromosome are displayed above each kymograph, with the labeled region indicated with a red triangle and its genomic position in degrees. Dashed lines superimposed to the kymographs provide a guide to the eye for the segregation pattern observed in the kymograph of HDR maxima in panel b (*ori*-HDR). N: number of nucleoids analyzed. Strains: HM923, HM673, BWX925, BWX1206, BWX1053.

(f) Simultaneous detection of HDRs and ParB-GFP. Left: typical two-color, representative 3D-SIM images of DAPI-stained single nucleoids and ParB-GFP-labeled origins for cells at different stages of the cell cycle. Nucleoid periphery is shown in light grey, while higher density regions at the center of the nucleoid are shown in dark grey. ParB-GFP complexes, localizing to the origins of replication, are represented in green. Right: 2.5D kymograph of HDRs with their density represented by the topography (z-axis). The superimposed colormap represents ParB-GFP intensity extracted from the same nucleoids. N: number of nucleoids analyzed. Strain: HM673. See also Fig. S5c.

(g) Re-localization of *ori*-HDRs during replication arrest and restart. Top: Two-dimensional distributions for cells synchronized in (left) G1-arrest and (right) 50 min after release of the replication block (nucleoid lengths between 1000-1250 nm and 1500-1750nm, respectively). Bottom: schematic representations depicting the localizations of *oriC* and *ter* as well as the right and left chromosomal arms from literature (Wang et al., 2014a). Strain: HM890. See also Fig. S5c.

Figure 6. Direct, 3D visualization of the organization of the origin domain.

(a-b) Representative (top) 3D-SIM and (bottom) 3D-PALM images of origins domains labeled with either ParB-GFP (green-red) or ParB-mEos2 (pink). For 3D-SIM images, the nucleoids were visualized by DAPI staining (grey contour), while for 3D-PALM imaging the cell volume was reconstructed from bright field images (dark grey contour). Panel a: the chromosome carries all naturally occurring *parS* sites (wild-type). Panel b: the chromosome carries a single *parS* site (*parS*³⁵⁹, strain *parS*-Δ7). Dotted square insets depict a schematic representation of the expected enrichment of fluorescently-labeled ParB-GFP within the origin domain for wild type and *parS*-Δ7. Strains: HM671, HM673, HM675 and HM677. See also Fig. S6a.

(c-f) 2.5D kymograph of ParB cluster distributions as a function of axial position and nucleoid length. The density of ParB clusters is represented by the topography of the kymograph (i.e. height in the z-axis). Color-codes applied to the kymograph and indicated on top of panels c and d represent either ParB cluster size (panel c and e) or the number of ParB-GFP sub-clusters (panel d and f). Insets in panels (e) and (f) depict a 2D view of the 2.5D kymographs with a color scale readjusted compared to WT, to highlight the ParB cluster migration pattern for cells having a single *parS*. Strains: HM671 and HM673. See also Figs. S6b-c.

Figure 7. Model of origin domain and chromosome organization during *B. subtilis* cell cycle.

(a) In nascent cells, the right and left replichores (in blue and red) are zipped (grey dotted lines) by the action of ParB/*parS* (orange hexagons) and SMC-ScpAB complexes (indicated in the figure). SMC-ScpAB proteins also are responsible for intra-arm pairing. Pink and yellow circles: oriC and DnaA boxes, respectively. The *ter* region is not yet resolved.

(b) During early replication, inter-arm contacts are disrupted to establish a G1-arrest-like configuration. This disruption can later propagate to the remainder of the chromosome. Grey/bright hexagons: replisomes.

(c) Re-organization of the origin region occurs concomitantly with origin migration to the middle of new nucleoids. Newly replicated origins are resolved by the action of the ParABS partition system and SMC-ScpAB. Left-right replichore pairing is reestablished at the origin domain. The recently replicated *ter* region starts to be resolved into the daughter cells.

(d) Origins are completely segregated to the nucleoid poles and the structures formed at nascent origin domains are propagated to the remainder of the chromosome possibly coupling chromosome segregation and cell division.

References

- Berkmen, M.B., and Grossman, A.D. (2006). Spatial and temporal organization of the *Bacillus subtilis* replication cycle. *Mol. Microbiol.* 62, 57–71.
- Berkmen, M.B., and Grossman, A.D. (2007). Subcellular positioning of the origin region of the *Bacillus subtilis* chromosome is independent of sequences within oriC, the site of replication initiation, and the replication initiator DnaA. *Mol. Microbiol.* 63, 150–165.
- Booker, B.M., Deng, S., and Higgins, N.P. (2010). DNA topology of highly transcribed operons in *Salmonella enterica* serovar Typhimurium. *Mol. Microbiol.* 78, 1348–1364.
- Breier, A.M., and Grossman, A.D. (2007). Whole-genome analysis of the chromosome partitioning and sporulation protein Spo0J (ParB) reveals spreading and origin-distal sites on the *Bacillus subtilis* chromosome. *Mol. Microbiol.* 64, 703–718.
- Cattoni, D.I., Fiche, J.-B., Valeri, A., Mignot, T., and Nollmann, M. (2013). Super-resolution imaging of bacteria in a microfluidics device. *PLoS ONE* 8, e76268.
- Dekker, J., Rippe, K., Dekker, M., and Kleckner, N. (2002). Capturing chromosome conformation. *Science* 295, 1306–1311.
- Dixon, J.R., Selvaraj, S., Yue, F., Kim, A., Li, Y., Shen, Y., Hu, M., Liu, J.S., and Ren, B. (2012). Topological domains in mammalian genomes identified by analysis of chromatin interactions. *Nature* 485, 376–380.
- Fiche, J., Cattoni, D., Diekmann, N., Mateos Langerak, J., Clerte, C., Royer, C.A., Margeat, E., Doan, T., and Nollmann, M. (2013). Recruitment, assembly and molecular architecture of the SpoIIIE DNA pump revealed by super-resolution microscopy. *PLoS Biol.* 11, e1001557.
- Fisher, J.K., Bourniquel, A., Witz, G., Weiner, B., Prentiss, M., and Kleckner, N. (2013). Four-dimensional imaging of *E. coli* nucleoid organization and dynamics in living cells. *Cell* 153, 882–895.

Gruber, S., and Errington, J. (2009). Recruitment of condensin to replication origin regions by ParB/SpoOJ promotes chromosome segregation in *B. subtilis*. *Cell* 137, 685–696.

Gruber, S., Veening, J.-W., Bach, J., Blettinger, M., Bramkamp, M., and Errington, J. (2014). Interlinked sister chromosomes arise in the absence of condensin during fast replication in *B. subtilis*. *Curr. Biol.* 24, 293–298.

Hadizadeh Yazdi, N., Guet, C.C., Johnson, R.C., and Marko, J.F. (2012). Variation of the folding and dynamics of the *Escherichia coli* chromosome with growth conditions. *Mol. Microbiol.* 86, 1318–1333.

Higgins, N.P. (2014). RNA polymerase: chromosome domain boundary maker and regulator of supercoil density. *Curr. Opin. Microbiol.* 22, 138–143.

Ishikawa, S., Ogura, Y., Yoshimura, M., Okumura, H., Cho, E., Kawai, Y., Kurokawa, K., Oshima, T., and Ogasawara, N. (2007). Distribution of stable DnaA-binding sites on the *Bacillus subtilis* genome detected using a modified ChIP-chip method. *DNA Res.* 14, 155–168.

Kleckner, N., Fisher, J.K., Stouf, M., White, M.A., Bates, D., and Witz, G. (2014). The bacterial nucleoid: nature, dynamics and sister segregation. *Curr. Opin. Microbiol.* 22, 127–137.

Kleine Borgmann, L.A.K., Ries, J., Ewers, H., Ulbrich, M.H., and Graumann, P.L. (2013). The bacterial SMC complex displays two distinct modes of interaction with the chromosome. *Cell Rep* 3, 1483–1492.

Le, T.B.K., Imakaev, M.V., Mirny, L.A., and Laub, M.T. (2013). High-resolution mapping of the spatial organization of a bacterial chromosome. *Science* 342, 731–734.

Lesne, A., Riposo, J., Roger, P., Cournac, A., and Mozziconacci, J. (2014). 3D genome reconstruction from chromosomal contacts. *Nat. Methods*.

Marbouty, M., Cournac, A., Flot, J.-F., Marie-Nelly, H., Mozziconacci, J., and Koszul, R. (2014). Metagenomic chromosome conformation capture (meta3C) unveils the diversity of chromosome organization in microorganisms. *Elife* 3.

Nasmyth, K., and Haering, C.H. (2009). Cohesin: its roles and mechanisms. *Annu Rev Genet* 43, 525–558.

Nicolas, P., Mäder, U., Dervyn, E., Rochat, T., Leduc, A., Pigeonneau, N., Bidnenko, E., Marchadier, E., Hoebeke, M., Aymerich, S., et al. (2012). Condition-dependent transcriptome reveals high-level regulatory architecture in *Bacillus subtilis*. *Science* 335, 1103–1106.

Okumura, H., Yoshimura, M., Ueki, M., Oshima, T., Ogasawara, N., and Ishikawa, S. (2011). Regulation of chromosomal replication initiation by *oriC*-proximal DnaA-box clusters in *Bacillus subtilis*. *Nucleic Acids Research* 40, 220–234.

Postow, L., Hardy, C.D., Arsuaga, J., and Cozzarelli, N.R. (2004). Topological domain structure of the *Escherichia coli* chromosome. *Genes Dev.* 18, 1766–1779.

Sexton, T., Yaffe, E., Kenigsberg, E., Bantignies, F.D.R., Leblanc, B., Hoichman, M., Parrinello, H., Tanay, A., and Cavalli, G. (2012). Three-dimensional folding and functional organization principles of the *Drosophila* genome. *Cell* 148, 458–472.

Smits, W.K., Merrikh, H., Bonilla, C.Y., and Grossman, A.D. (2011). Primosomal Proteins DnaD and DnaB Are Recruited to Chromosomal Regions Bound by DnaA in *Bacillus subtilis*. *J. Bacteriol.* 193, 640–648.

Smits, W.K., and Grossman, A.D. (2010). The transcriptional regulator Rok binds A+T-rich DNA and is involved in repression of a mobile genetic element in *Bacillus subtilis*. *PLoS Genet.* 6, e1001207.

Soh, Y.-M., Bürmann, F., Shin, H.-C., Oda, T., Jin, K.S., Toseland, C.P., Kim, C., Lee, H., Kim, S.J., Kong, M.-S., et al. (2015). Molecular basis for SMC rod formation and its dissolution upon DNA binding. *Mol. Cell* 57, 290–303.

Sullivan, N., Marquis, K., and Rudner, D. (2009). Recruitment of SMC by ParB-*parS* organizes the origin region and promotes efficient chromosome segregation. *Cell* 137, 697–707.

Umbarger, M.A., Toro, E., Wright, M.A., Porreca, G.J., Baù, D., Hong, S.-H., Fero, M.J., Zhu, L.J., Marti-Renom, M.A., McAdams, H.H., et al. (2011). The Three-Dimensional Architecture of a Bacterial Genome and Its Alteration by Genetic Perturbation. *Mol. Cell* 44, 252–264.

Wang, X., Montero Llopis, P., and Rudner, D.Z. (2014a). *Bacillus subtilis* chromosome organization oscillates between two distinct patterns. *Proc. Natl. Acad. Sci. U.S.A.* 111, 12877–12882.

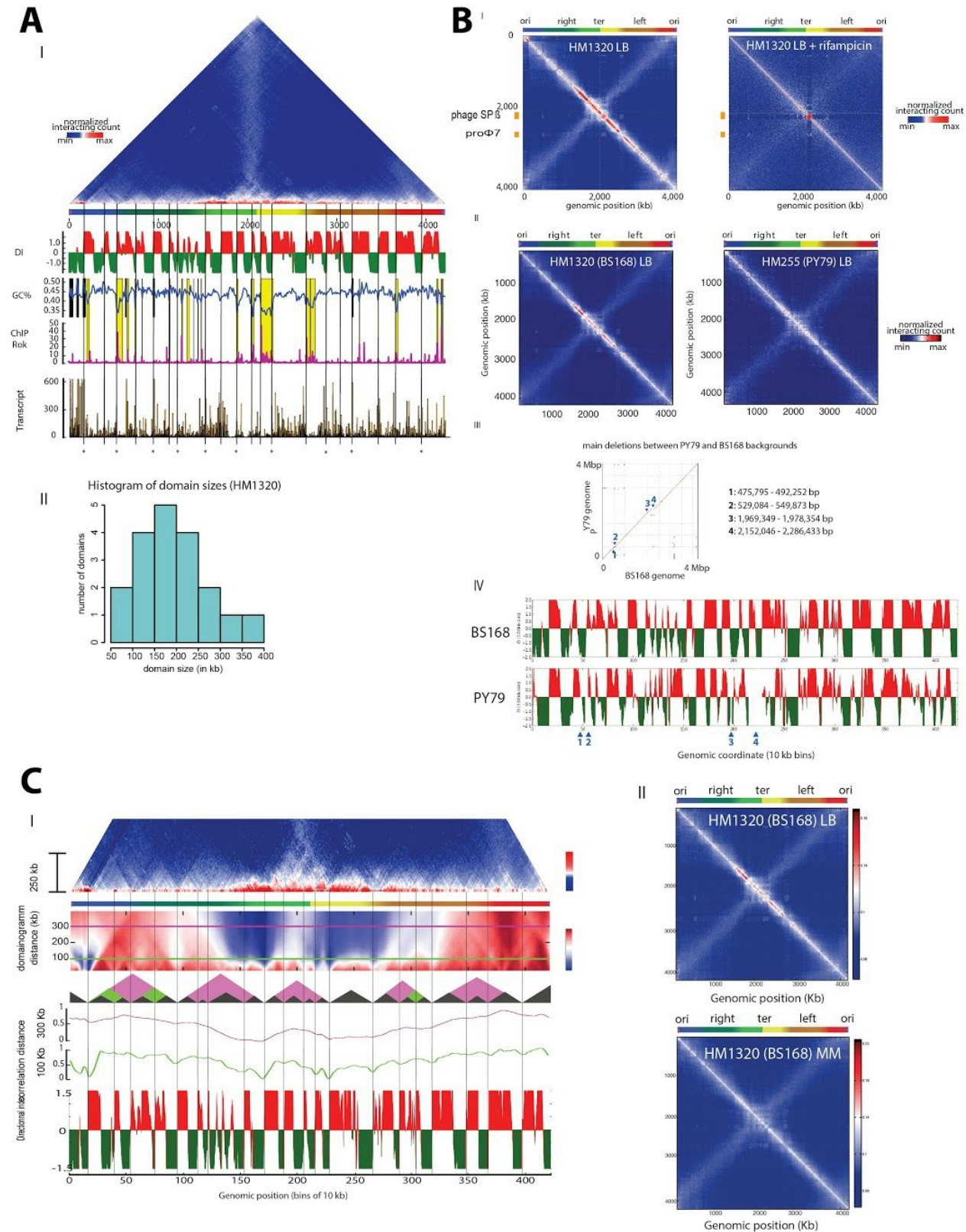
Wang, X., Tang, O.W., Riley, E.P., and Rudner, D.Z. (2014b). The SMC condensin complex is required for origin segregation in *Bacillus subtilis*. *Curr. Biol.* 24, 287–292.

Index

This supplement contains:

- Extended data
- Supplemental Experimental Procedures
- References

Figure S1. Analysis of Hi-C map, related to Fig. 1.



Panel A: Directionality index analysis, and correlation of frontiers with highly transcribed genes, gene acquired through horizontal transfer, and Rok occupancy.

I. We investigated the potential links between the presence of highly expressed genes (HEG), variations in GC content (essentially DNA regions acquired through horizontal gene transfer, such as prophages) and Rok occupancy (Smits et al. 2010) with the positions of the barriers between domains detected by directional index analysis (HM1320, LB conditions). From top to bottom: normalized genome-wide contact map (HM1320 in rich media); Directionality index analysis; GC content (4kb window); Enrichment for the Rok protein (Smits and Grossman, 2010); transcription signal (Rasmussen et al 2009). 20 significant barriers were detected at the following positions (in kb): 160, 390, 530, 740, 940, 1120, 1210, 1520, 1700, 1880, 2050, 2150, 2270, 2650, 2880, 3020, 3170, 3460, 3670 and 3960 along the chromosome. For transcription analysis, we mapped against the BS168 reference the reads of a RNA-seq dataset [SRX315309] obtained with a *B. subtilis* wild-type strain growing in LB genome and binned the raw signal into 2kb windows. The 5 % of these 2kb bins that presented the highest transcription signal were considered as HEG (104 in total). Whereas among the 422 10kb bins in the HM1320 contact map (Figure 1a), 73 contained a HEG (17.2%), this ratio raised to 55% (11 instances) when considering only the bins corresponding to the 20 barriers detected by DI analysis (significant enrichment, Fisher test p-value =0.002). Among the 9 remaining barriers, we observed a high correlation with Rok (7 barriers), a factor that binds specifically to regions with divergent GC content (HGT regions). One should notice that in the *Caulobacter crescentus* genome, the few horizontal transfer elements present are also responsible of a the generation of barriers (data not shown). Finally, one barrier correlated with the presence of a very long coding gene (position: 390 kb), and a different one did not correlate with any of these factors. Phages and AT-rich regions (i.e. HGT regions) are indicated as yellow boxes, whereas rRNA clusters are shown as black vertical lines. Asterisks indicate a barrier correlating with a highly expressed gene (identity indicated below transcription profile).

II. Distribution of distances between barriers detected from directional index analysis. The positions of barriers are shown in panel I.

Panel B: Contact maps are affected by treatment with rifampicin but not by genetic background.

I. Normalized genome-wide contact maps for HM1320 in rich medium (LB, left) and HM1320 in rich medium + rifampicin (right). Phages are annotated on the side of the matrixes. Barriers between CIDs are considerably disturbed when cells are treated with rifampicin, indicating a role of active transcription in the formation of barriers (see left and right matrices in Figure S1b-I). This role may be partly direct, as suggested for *E. coli* (Booker et al., 2010) and *C. crescentus* (Le et al., 2013). However, it is worth noting that rifampicin treatment will also affect gene expression and protein production. These may very likely influence other cellular processes that play a key role in chromosome structure, such as the maintenance of the appropriate levels of negative supercoiling, DNA condensation by nucleoid associated proteins, or DNA replication. Thus, treatment of cells by rifampicin will affect many cellular processes at the same time, making a clear-cut conclusion on the specific role of transcription in the formation of barriers between CIDs difficult to make.

II. Two different strains of *B. subtilis*, PY79 (Youngman et al., 1983) and BS168 (Kunst et al., 1997), have recurrently been used as wild-type references in the past. Because the mutations analyzed in this study have been generated in these two genetic backgrounds, we compared genomic contact maps of strains HM1320 and HM255 (BS168 and PY79 genotypes, respectively) grown in rich medium (left and right panels, respectively). Vertical and horizontal axis represent chromosomal and genomic positions centered on the terminus of replication, with the left and right arms represented by red-to-yellow and blue-to-green gradients (from ori to ter), respectively. The origin is represented as pink semi-circles. This color code is conserved across all panels of all figures to facilitate reading.

III. To compare CIDs between backgrounds, we first aligned the two genomes against one another, to identify the major differences between them (panel III). Reference genomes were aligned using the MUMmer software 3.0 (Kurtz et al., 2004) and represented as Dot-plot alignments (see Supplemental Experimental Procedures). The four largest deletions (numbered 1 – 4) present in the PY79 background as compared to BS168 are indicated on the right. The four largest structural variations were taken into account when aligning the genomes for subsequent DI analysis: a large (134kb) prophage insertion in the genome of BS168, and three smaller (~10kb) deletions (Nicolas, 2002).

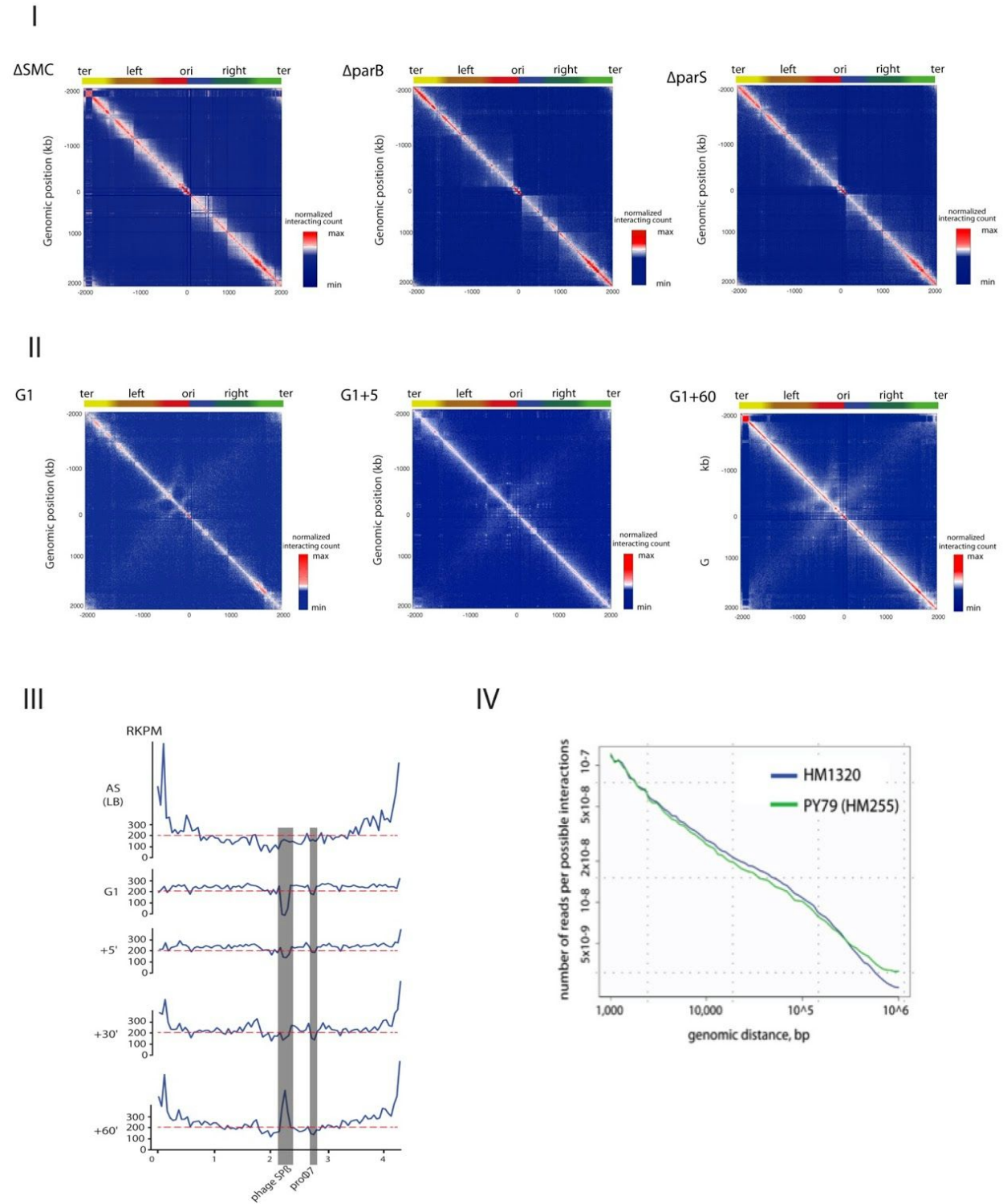
IV. CIDs were identified by computing the directional index (DI) profiles of strain HM1320 (BS168 background) and of HM255 (PY79 background) in rich medium. These profiles are fairly similar between the two genetic backgrounds, aside from regions where large deletions or insertions occurred.

Panel C: Comparison of Directionality Index (DI) and Domainogram analysis, and Hi-C matrices in rich and minimal medium.

I. Comparison between domainogram and directionality index analyses. From top to bottom: contact matrix of HM1320 strain; multiscale domainogram, representation of domain detected by DI (grey triangle), 100Kb domainogram (green triangle) and 300 Kb domainogram (purple triangle); 300 Kb domainogram; 100KB domainogram; DI. Green and purple lines represent the density pattern of the domainogram at window sizes 100 and 300 kb. At smaller sizes, patterns that are highly consistent with the DI analysis appear (see green line - 100 Kb). At the larger scale (purple line - 300Kb), the pattern reflects the presence of large domains within the contact map, which are not clearly apparent in the DI analysis.

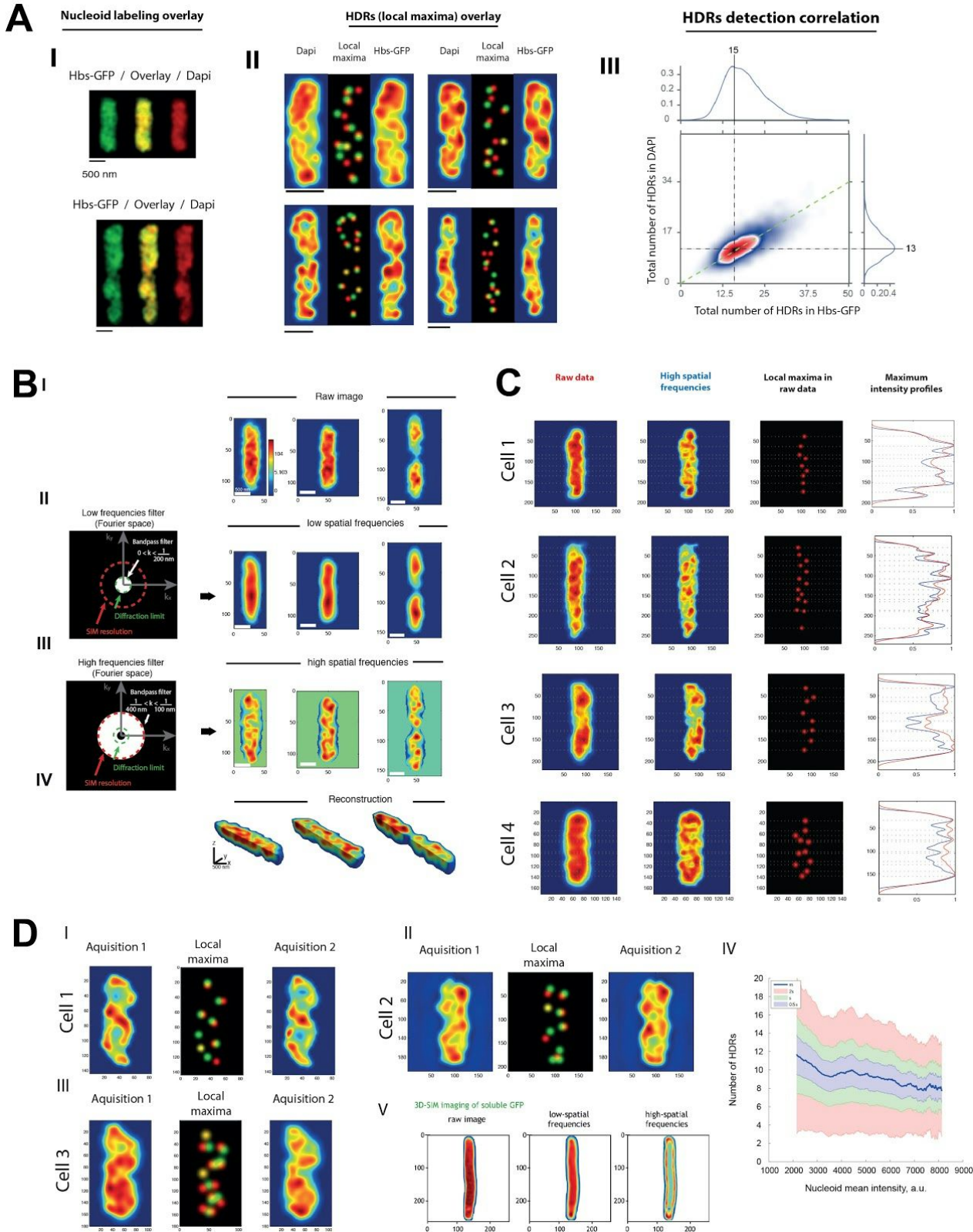
II. Genomic contact maps of strains HM1320 grown in (left) rich and (right) minimal media. Vertical and horizontal axis represent the chromosome and genomic positions centered on the terminus of replication, with the left and right arm represented by red to yellow and blue to green gradients (from ori to ter), respectively. Large scale features, such as the presence of a secondary diagonal and inter-arm hairpin, are unaffected by growth medium, consistent with replicore pairing and origin folding being conserved independently of growth rate.

Figure S2. Full Contact maps of SMC, ParB and parS- Δ 10 strains, and replication-arrested cells. Read coverage, and effect of a GFP tag on Hbs on chromosome organization, related to Fig. 3.



- I. Normalized contact maps centered at *oriC* for SMC-depleted cells (left), Δ parB (middle), and Δ parS (right) mutants. Top axis: same color-code for chromosome representations as in Figure 1. Strains: AK487, AK525 and AK215.
- II. Full, normalized contact maps centered at *oriC* for dnaB-ts cells arrested in G1 (left) and released at permissive temperature into S-phase after (middle) 5, and (right) 60 minutes. Top axis: same color-code for chromosome representations as in Figure 1. Strain: HM890.
- III. Read coverage along the chromosome was plotted for fast dividing cells growing in rich medium (top) and for synchronized cells (HM890) as they were released into S-phase (G1, 5, 30 and 60 minutes) (see Supplemental Experimental Procedures). The x-axis represents the genome coordinates and the y-axis indicates the number of Reads Per Kb per million mapped reads (RPKM). Red dotted line at 200 rkpm aims at facilitating comparison between time points. Prophages distinguish themselves from the rest of the genome. The phage SP β in particular appears over replicated after one hour, consistent with its excision and independent amplification in at least a fraction of the cells, maybe as a consequence of the incubation at the restrictive temperature.
- IV. To investigate whether the addition of a GFP tag to Hbs produced affected long-range contacts, we plotted the frequency of interactions as a function of genomic distance separation for wild-type (PY79) and HM1320. No significant difference could be identified in the contact frequency, consistent with HM1320 behaving like wild-type at the resolution of our 3C experiments.

Figure S3. Detection and characterization of High Density Chromosomal Regions, related to Fig. 4.



Panel A: Comparison between Hbs-GFP and DAPI whole-chromosome labeling

I. Homogeneous labeling of the whole *B. subtilis* chromosome was obtained through two high-density labeling strategies: Hbs-GFP and DAPI staining (see Supplemental Experimental Procedures). Image shows two two-color 3D-SIM representative images of nucleoids simultaneously labeled with Hbs-GFP and DAPI. Image acquisition was performed sequentially for each fluorophore starting with the GFP fluorescence channel. Maximum projections along the Z axis of the 3D volumes are shown in green and red for Hbs-GFP and DAPI channels respectively. Overlay of the 2 channels is represented in between: yellow regions of the overlay highlight overlap of the Hbs-GFP tag and DAPI staining whereas red or green regions reveal areas with no overlap.

II. HDR detection in sequential two-color 3D-SIM of four representative nucleoids labeled by Hbs-GFP and DAPI (left and right panels, respectively). HDRs identified through local maxima detection in each volume are represented in 2D as Gaussians of 100nm width (in red and green for DAPI and Hbs-GFP respectively). HDRs that did not move between the successive acquisitions will show up as overlapping Gaussians and will appear in yellow. The integration time in our fastest 3D-SIM imaging conditions for two colors was ~20 s per channel (i.e. total imaging time ~50 s). The number and positions of detected HDRs in individual nucleoids did not vary significantly between the two colors. Note that due to nucleoids dynamics between the successive acquisitions and our temporal resolution, most HDRs will slightly change their locations but a strong correlation between their positions can still be noted. This observation is consistent with previous studies showing that the overall shape of bacterial nucleoids is stable over minutes while sub-nucleoid patterns display fluctuations at the ~1 min timescale (Hadizadeh Yazdi et al., 2012).

III. To further compare these full-chromosome labeling strategies, we quantified the distribution in the number of detected HDRs during slow growth for nucleoids simultaneously labeled with both strategies. The relationship between the distributions in the number of HDRs detected in sequential two-color 3D-SIM of nucleoids labeled by Hbs-GFP and DAPI is represented as a 2D Kernel density histogram. The highly linear relationship between the numbers of detected HDR per nucleoid in the two colors reveals a strong correlation between the 2 labeling strategies.

Panel B: HDR visualization and Fourier space decomposition.

I. Raw 3D-SIM nucleoid images from the middle plane of four representative cells (DAPI stain, Strain: PY79). The mixture of both low and high spatial frequencies makes sub-diffraction structures difficult to observe.

II. 3D volumes in panel I were low-pass filtered using a 3D Butterworth low-frequency filter with a spatial cutoff at 200 nm (see left panel) to simulate the absence of high spatial frequencies typical in conventional microscopy images. In this case, nucleoids resembled images typically obtained by wide-field microscopy (Hadizadeh Yazdi et al., 2012; Wang, et al. 2014).

III. 3D volumes in panel I were band-passed filtered using a 3D Butterworth band-pass filter with spatial cutoffs at 100 and 400 nm (see left panel). The increase in resolution gained by 3D-SIM is apparent in these images. When higher-spatial frequencies are considered, nucleoids display a continuous filament-like structure. Because of the ordered choreography of the *B. subtilis* chromosome, we expect contiguous genomic loci to display proximal spatial positions. This specific correlation between genomic sequence and sub-cellular localization is consistent with our observation that high-density regions are joined by continuous density bundles that stretch along the long axis of the nucleoid. Similar longitudinal density bundles have previously been reported in other bacteria (Fisher et al 2013). It is worth mentioning that nucleoids often display semi-continuous helical filaments that can be observed in the high spatial frequency reconstruction (see representative nucleoids in Figure S3). However, this feature is not characteristic of all nucleoids observed in our experimental conditions.

IV. 3D-SIM images of the same nucleoids as in panel (I) with the full spatial frequencies shown in panels II and III and with higher spatial frequencies enhanced.

Panel C: Detection of HDRs from raw 3D-SIM images.

I. Visualization and detection of HDRs in single nucleoids (see Supplemental Experimental Procedures). Four representative nucleoids are shown to illustrate HDRs and their detection in single nucleoids. Left column represents maximum intensity projections of nucleoids stained with DAPI in wild-type cells (PY79) and without any spatial frequency enhancement. Second column represents the same nucleoids with high spatial frequencies enhanced to help the visualization of HDRs. Third column represents HDRs identified through local maxima detection in nucleoid volumes represented in the first column and plotted as 2D red Gaussians. Fourth column represents the nucleoid long axis intensity profiles integrated over ~half the nucleoid width. These profiles are shown to give an indication of the achieved signal to noise ratio of the detected HDRs from the processed and non-processed images (blue and red solid lines, respectively corresponding to intensity profiles from images in the first and second columns).

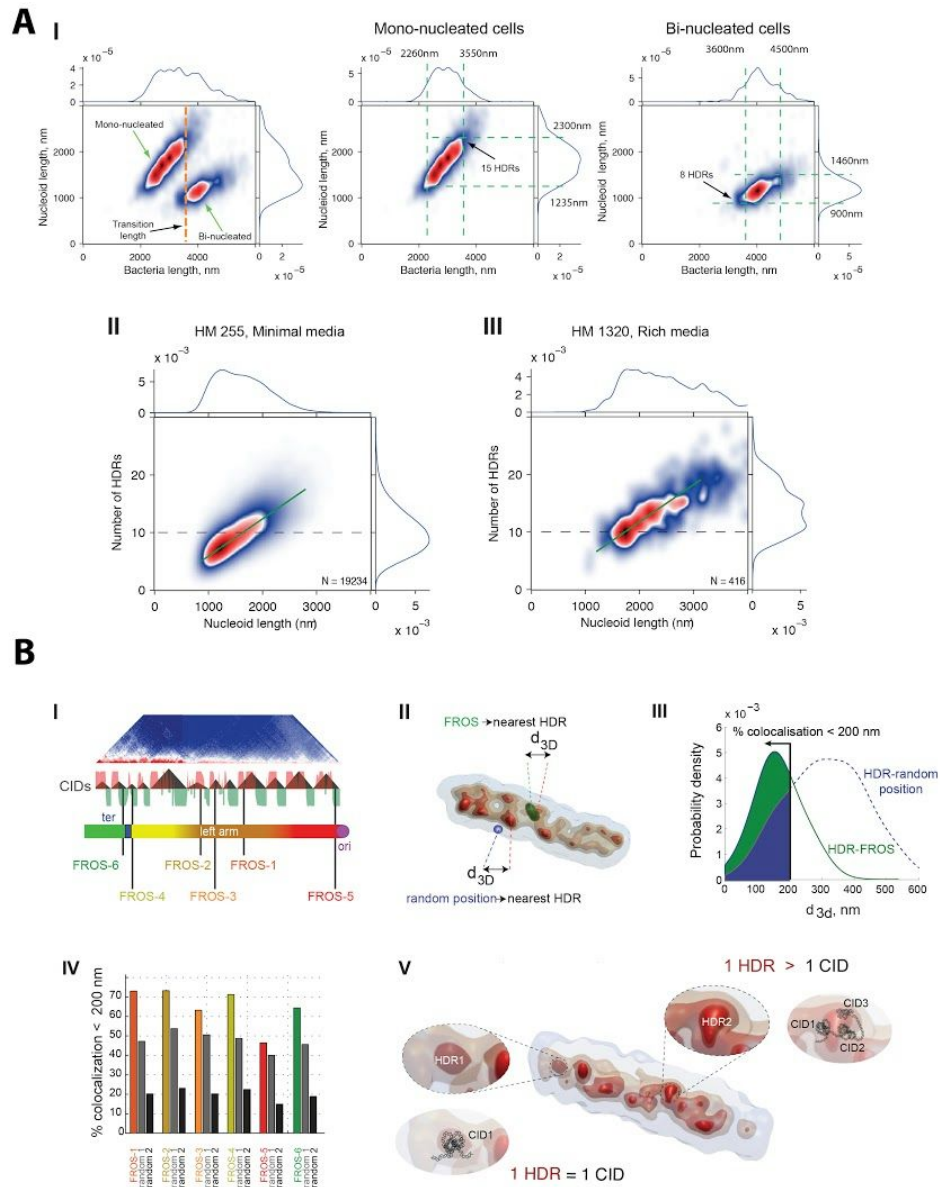
Panel D: 3D-SIM time-lapse acquisition for DAPI-stained nucleoids, 3D-SIM imaging of cytosolic GFP, and analysis of number of HDRs versus nucleoid intensity.

I-III. As a further validation of our whole-chromosome labeling strategy and HDR detection method, we conducted time-lapse experiments of DAPI-stained nucleoids by sequential acquisition. In each subpanel, left and right images represent nucleoids maximum projection along the Z axis for 2 successive acquisitions of the same nucleoids (acquisition 1 and 2, left and right panels respectively). The overall nucleoid morphology is conserved between the images revealing only small dynamical changes between acquisitions. Central panels depict the detected HDRs in each acquisition using our local maxima detection algorithm. Local maxima detected in the first and second acquisitions are color-coded in red and green respectively, while overlapping HDRs in both acquisitions are color-coded in yellow. Sequential acquisitions display strong correlation between their HDRs number and positions. Small variations in their position and intensities can still be observed, reflecting the internal dynamics of the nucleoid between acquisitions. These dynamics are consistent with previous analysis in *E. coli* using conventional microscopies (Fisher et al. 2013, HadizadehYazdi et al 2012). Each panel (I to III) represents a different cell.

IV. To assess the effect of noise on the counting of detected HDRs, we computed the number of detected HDRs as a function of the mean nucleoid intensity. The signal to noise ratio (SNR) is proportional to the intensity in the nucleoid, with the SNR in low intensity nucleoids being in all cases >10 . The plot shows that the number of detected HDRs is almost independent on nucleoid intensity, with very bright nucleoids having a similar number of HDRs than low-intensity nucleoids. Thus, these data are consistent with the detected HDRs not being influenced by the detection of high-frequency noise in the data.

V. To ensure that HDRs were not the result of the reconstruction algorithm amplifying noise from low signal-to-noise ratios intensity profiles, we expressed cytosolic GFP on anucleated *B. subtilis* cells (obtained by treatment with mitomycin C 50 ng/ml during 30 min) and image them using the same parameters as those used to image whole labeled chromosomes. We observed very low fluctuations in intensity in the raw image (left) a flat fluorescence signal at low-frequencies (middle), and high-frequency signal exclusively in the frontier between cytosol and membrane (right) where the signal drops to zero. These images were dramatically different to those observed for Hbs-GFP or DAPI-stained nucleoids (see for instance Figure S3).

Figure S4. Distribution and interpretation of HDRs, related to Fig. 4.



Panel A: The life cycle of a nucleoid within the cell cycle of the cell.

I. Analysis of ParB and HDRs localization was performed by using the coordinate system of the nucleoid, not that of the cell. The use of nucleoid coordinates allowed better accuracy in the relative positions of different structures for two reasons: (1) the signal-to-noise ratio of the nucleoid intensity signal was considerably larger than for the cell membrane/cell wall (obtained through bright field imaging); and (2) segmentation of non-overlapping 3D volumes was considerably more robust, as nucleoids of neighboring cells are well separated while signals from membranes/cell walls of neighboring cells are partially overlapping. This choice, however, was not without inconvenience, as the smallest detected nucleoids represent a mix between nucleoids segmented in newborn cells, or in cells that have split their nucleoid after replication and segregation, but have still not divided. In panel I, we evaluated the contribution of mono-nucleated and bi-nucleated cells to the distribution of nucleoid sizes and the number of HDRs by plotting the distribution of nucleoid vs. cell length for cells growing in minimal media. Nucleoids and cell contours (based on bright field images) of cells growing in minimal medium were simultaneously segmented, and a 2D distribution of the

correlation between nucleoid and cell lengths was plotted. **Left panel:** distribution of nucleoid sizes as a function of cell size in an asynchronous wild-type population (HM923 strain; N = 3201). Two distinct populations were observed. First, a group where cells and nucleoid lengths increase proportionally until cells reach sizes of $\sim 3.6 \mu\text{m}$, where an abrupt transition occurs (see orange dashed line in left panel) leading to a second group of longer cells with smaller nucleoids. This represented the transition from mono-nucleated cells to bi-nucleated cells. **In middle and left panels,** we segmented cells containing one (N = 1991) or two (N = 1210) nucleoids and built the same kind of distribution plot (middle and right panels, respectively). Green dashed lines indicate the approximated full width half maximum of the distributions and the ranges of nucleoid and cell sizes. The number of HDRs for the largest and smallest nucleoids is indicated in the middle and right panels. Mono-nucleated cells contained nucleoids ranging from 1.2 to 2.3 μm (middle panel) while bi-nucleated cells showed smaller nucleoids ranging from 900 to 1400 nm (right panel). Nucleoids in bi-nucleated cells represented $\sim 40\%$ of the total distribution of nucleoids in asynchronous cells. This analysis indicates that nucleoid splitting occurs before cell division as it was previously reported. Thus, the smallest detected nucleoids (length $> 0.9 \mu\text{m}$) live in bi-nucleated cells and represent newborn nucleoids, while the largest detected nucleoids ($\sim 2.3 \mu\text{m}$ in length) are detected in mono-nucleated cells that have not yet undergone division. Newborn nucleoids contained in average 7.9 ± 2.1 HDRs, while the largest nucleoids before nucleoid splitting contained 15 ± 4 HDRs, consistent with a doubling in the number of HDRs during the life cycle of the nucleoid (indicated in middle and right panels).

II-III. Density plots representing the number of HDRs vs. nucleoid length for cells growing in (left panel) minimal medium (PY79, strain HM255, N=19234) and (right panel) rich medium (strain HM1320, BS168 background, N=416). Green solid and black dashed lines were plotted to facilitate visual comparison between panels. These distributions reflect the average and heterogeneity in the number of HDRs in a cell population. Note that nucleoids in rich medium are larger and display a higher number of HDRs, even for the smallest nucleoids detected. In rich medium, newborn nucleoids ($\sim 1.5 \mu\text{m}$ in length) contained in average 9.5 ± 1 HDRs, while the largest nucleoids ($\sim 3.7 \mu\text{m}$ in length) before nucleoid split contained 18.5 ± 2 HDRs. These results are consistent with cells growing in rich media containing a larger amount of DNA due to multiple replication cycles taking place simultaneously (Sharpe et al., 1998). Interestingly, the rate of increase in the number of HDRs with nucleoid length (green solid line) was weakly dependent on growth medium.

Panel B: Detection of FROS tags within CIDs.

I. The existence of a higher-order nucleoid sub-organization has not previously been reported. It is thus of interest to know whether/how HDRs are related to genomically-specified organizational features. CIDs comprise DNA domains presenting enriched contacts and are thus expected to be present in condensed regions within the cell. However, HDRs are substantially larger than the average CID as defined above. We therefore imagine that HDRs may often represent stochastic associations of CIDs. In an attempt to gain further insight on this hypothesis, we labeled six different CIDs by using fluorescent repressor operator arrays (FROS) tags and measured the distribution of distances between FROS tags and the most proximal HDR. Top panel represents the magnification of the Hi-C contact map within the left arm of the chromosome (45° clockwise rotation), the middle panel shows the DI analysis of the corresponding region with schematic representations of domains (grey triangles), and the lower panel displays the genomic annotations of the designed FROS tags. Two FROS were located in CIDs close to the Terminus region of the chromosome, one CID near the origin and three others along the left replicore. FROS tags coordinates were: 359° , 273° , 256° , 240° , 181° and 174° .

II. 3D-SIM imaging of these tags resulted in bright, resolution-limited foci whose center of mass can be located with voxel precision (39.5 nm in X and Y, 125 nm in Z). For each detected FROS tag (green spot, FROS-1 for this example) its 3D distance (d3D) to the closest HDR is calculated. This process was repeated for each individual nucleoid of each cell line containing a different FROS tag. A negative control is performed in a similar manner where a locus is randomly generated (blue spot) within the same nucleoid volume and its distance to the closest HDR calculated. We used two different negative controls. The first consisted of randomly choosing a FROS position within the volume of each nucleoid for which a real FROS-HDR distance was measured. In this case, the nucleoid volume was considered homogeneous (control 1). In the second control, the localization probability of the random FROS was proportional to the real volumetric fluorescence

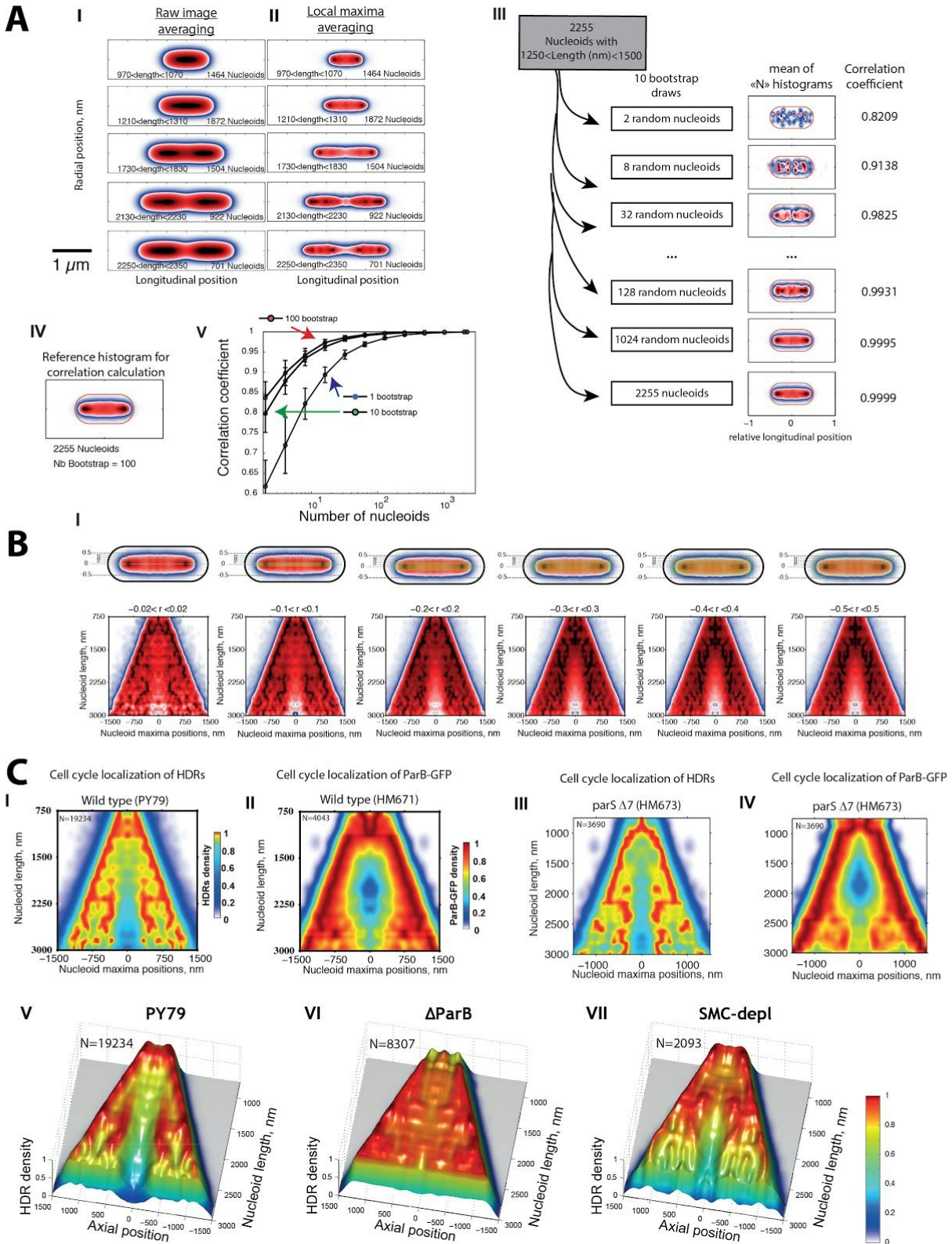
intensity signal of the nucleoid (control 2). This second control accounts for inhomogeneous variations in nucleoid density. For both controls, we measured the distance of the simulated FROS position to the closest HDR.

III. Distributions of d3D distances for both the experimental FROS tag and the simulated tags were obtained. Typical kernel density estimation of these distributions for the FROS tag (green line) and the random locus (blue line) are shown. To extract a degree of co-localization, we quantified in each case the percentage of distances smaller than 200 nm (chose as a compromise between the maximal lateral and axial resolutions of 3D-SIM: 120 and ~300 nm).

IV. Summary of co-localization percentages for all probed FROS tags (colored bars) with their corresponding controls (grey and dark bars for tags locations accounting for the real volumetric DNA density and tags assuming a homogeneous nucleoid DNA density, respectively). Notably, the positions of experimental FROS tags were significantly correlated with the localization of HDRs, since for all the measured FROS tags the degree of co-localization was between ~50 and 70%. In contrast, the associated negative controls yielded co-localizations below 20% (control 1) or 50% (control 2). In all cases, the experimental co-localization was larger than the control.

V. These significant correlations are consistent with HDRs representing stochastic groupings of single or multiple CIDs .

Figure S5. Analysis of HDR and FROS kymographs, related to Fig. 5



Panel A: 2D histograms of HDR positions.

I. To determine whether the positions of HDRs are conserved within the nucleoid, we first averaged 3D images of nucleoids of comparable lengths (corresponding to similar stages of the cell cycle, Strain: PY79, DAPI staining). Different rows represent different nucleoid sizes. The overall nucleoid morphology is well recovered with nucleoids of length higher than ~1700 nm displaying a bilobed shape. High DNA densities (black) are clearly visible along the longitudinal axis of the nucleoid while lighter DNA density regions are localized at the nucleoid periphery (blue). This procedure, however, averages out the spatial features observed in single nucleoids by 3D-SIM.

II. Averaging of HDR positions (Strain: PY79, DAPI staining; see Supplemental Experimental Procedures for details). By directly averaging HDRs, the signal to noise ratio of HDR localization can be enhanced, as this procedure removes the background signal from regions of the nucleoid without DNA enrichment.

III. Procedure used to assess the robustness of 2D histograms and kymographs. Nucleoids with a size comprised between 1250 – 1500 nm were used to assess the robustness of 2D histograms and estimate the minimal number of nucleoids necessary to sample cell heterogeneity in a population (PY79, Strain HM255, DAPI staining). First, the reference histogram is built (see panel IV). Then, increasing amount of nucleoids (2, 4, 8...2048) were pooled together and resampled N times ($N=1, 10$ or 100). The resulting mean histograms for each pool were correlated to the reference histogram to get a correlation coefficient (right column). From 2 to 32 selected nucleoids, no clear pattern can be observed. From 32 to 128 nucleoids, the polar signature of the origin HDR appears but the overall pattern of localization is neither robust nor exempt from artifacts. From 128 to 512 nucleoids, only the origin HDR exhibits a discrete localization that does not vary when more nucleoids are added to the pool.

IV. All nucleoids with a size comprised between 1250 – 1500 nm were considered to compute a “reference” histogram by resampling 100 times (bootstrap draws) the selection of nucleoids from a total of 2255 nucleoids, and then calculating the mean of the 100 obtained histograms.

V. Resulting correlation coefficients for three different bootstrap draws values (1, 10 and 100) are plotted against the initial number of nucleoids selected. Error bars represent the standard deviation for 100 iterations of the procedure described in the upper panel. When 1 bootstrap resampling or no resampling was performed, more than ~500 initial nucleoids were required to compute a robust histogram of HDRs localizations. Increasing the number of bootstrap draws to 100 reduced the initial minimum statistics to a hundred of nucleoids. This approach illustrates how the heterogeneity in HDR localizations in different nucleoids can be fully explored while minimizing the initial required statistics. In addition, this approach provides a way to assess the robustness of the resulting histograms.

Panel B: Integration of HDRs localizations using different radial windows and percentage of HDRs within different radial distances.

I. Kymographs were computed for six increasing radial integration windows of the nucleoid volume from the same pool of 13,503 nucleoids (PY79, Strain: HM255, DAPI stain). Kymograph k contained HDRs localizations satisfying $|r| < r_k$, with r representing the radial distance and r_k the maximal radial integration window in normalized units (with $r_k = 0.02, 0.1, 0.2, 0.3, 0.4, 0.5$ integrating 19, 51, 79, 95, 99 and 100% of HDRs respectively). In this panel, the different integration windows represent, from left to right, 4% ($|r| < 0.02$) to 100% ($|r| < 0.5$) of the nucleoid width respectively. Above each kymograph, the corresponding relative radial positions in which HDRs detections were integrated are indicated (shaded yellow areas). The polar positions of origin HDRs are visible throughout the sections in which $|r| < 0.2$ (i.e. within 40% of the central part of the nucleoid volume). Larger integration windows do not display a distinct signature that can be associated with the origin (Figure 5b). Colormap of HDRs density is indicated on the bottom right of the figure.

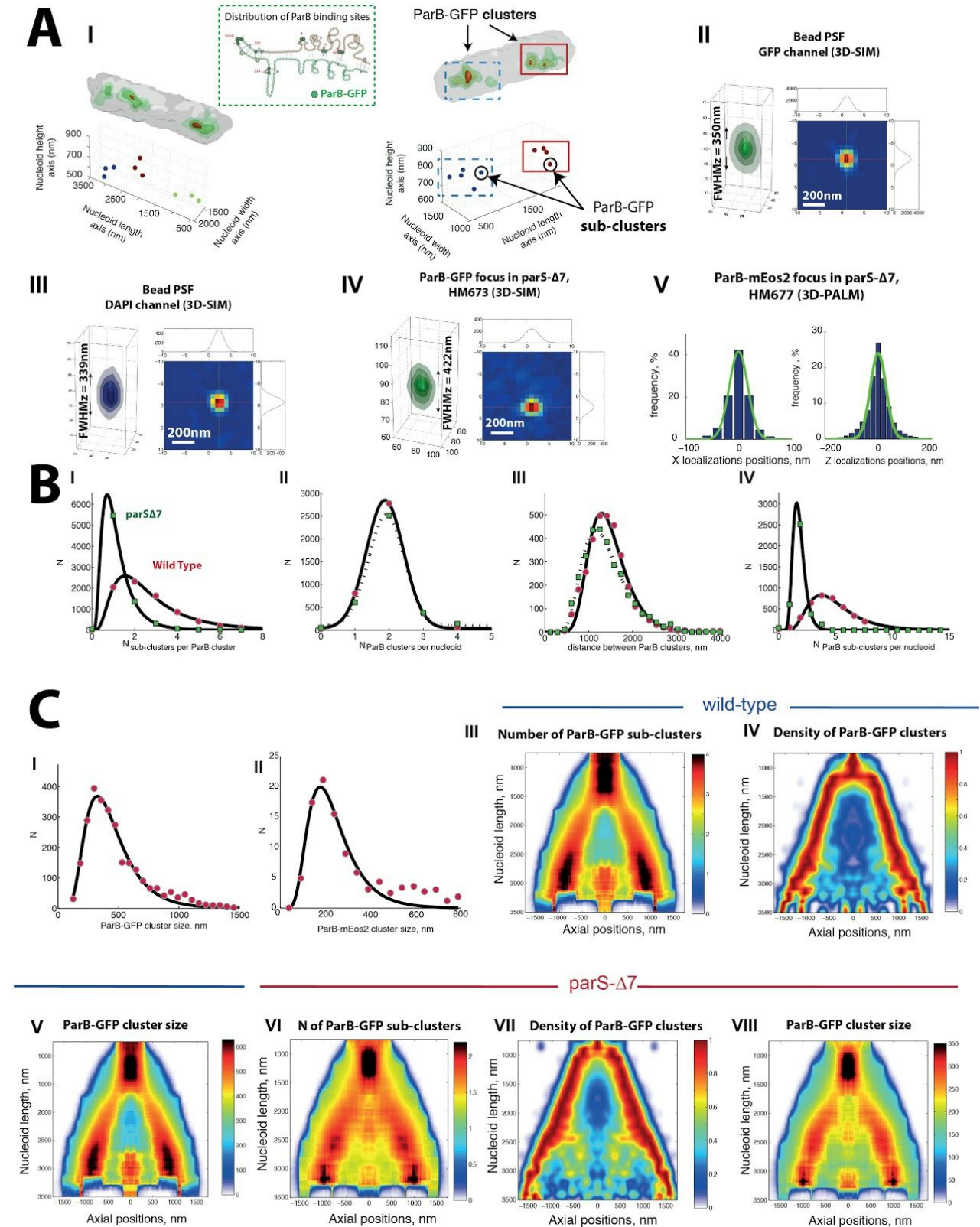
Panel C: and 2.5D kymographs of HDRs localizations for wild type and mutants.

I, III: HDRs localization (I) in DAPI-labeled nucleoids for wild-type cells with all naturally-occurring *parS* sites (PY79), (III) in DAPI-labeled nucleoids for cells with 1 *parS* site (*parS* Δ 7, HM673).

II, IV: ParB-GFP localization (II) in wild-type cells with all naturally-occurring *parS* sites (HM671), (IV) in cells with 1 *parS* site (*parS* Δ 7, HM673).

V-VII. HDR localization (V) in DAPI-labeled nucleoids for wild-type cells with all naturally-occurring *parS* sites (PY79, strain HM255), (VI) in DAPI-labeled nucleoids for cells devoid of ParB (Δ ParB; strain HM525), (VII) in DAPI-labeled nucleoids for SMC-depleted cells (SMC-depl; strain AK488). In absence of ParB or SMC, the kymographs are perturbed yet still display an overall HDR localization pattern resembling that of wild-type cells. These results are consistent with abnormal chromosome segregation patterns in the absence of ParB or SMC, but reveal that they do not seem essential for the polar positioning of origin HDRs in these growth conditions.

Figure S6. Analysis of origin domain dynamics probed by ParB-GFP, related to Fig. 6.



Panel A: The origin domain is composed of several ParB-GFP sub-clusters and estimation of empirical resolution of 3D-SIM and 3D-PALM.

I. Origin domains were visualized by super-resolution in live cells using ParB-GFP as a proxy. Several sub-clusters of ParB-GFP were observed most of the time within each ParB cluster. Top panel: two representative examples of 3D-SIM live imaging of cells with DAPI-labeled nucleoids (in grey) and origin domain labelled by ParB-GFP (in green and red for different isolevels; strain HM671). Several ParB-GFP sub-clusters were observed to compose each ParB cluster (see annotation in the top right panel). Bottom panel: 3D representation of the ParB-GFP sub-clusters identified in each origin domain on similar nucleoids (see Supplemental Experimental Procedures for further details on the 3D-SIM cluster detection algorithm). Each bead represents a single ParB-GFP sub-cluster. Beads of the same color have been annotated as belonging to the same ParB cluster identifying an individual origin domain (see Supplemental Experimental Procedures for details). Boxed inset on the rightmost panel shows distribution of ParB-GFP binding sites at the origin domain.

II-III. The Full Width at Half Maximum (FWHM) was measured in 3D-SIM on fluorescent beads fixed on a coverslip for different excitation and emission wavelengths matching GFP and DAPI spectra. 3D point spread function (PSF) of fluorescent beads imaged in the GFP (II) and DAPI (III) channels (with emission peaks at 504 nm and 461 nm, respectively). 2D Gaussian fits in the XYZ directions yielded a FWHM of 111, 127 and 350 nm for GFP and 111, 124 and 339 nm for DAPI, corresponding to a doubling of the maximal resolution of standard epi-fluorescence imaging.

IV. Resolution was also measured by imaging with 3D-SIM a single cluster of ParB-GFP in live cells (HM673 strain, *parS*- $\Delta 7$, single *parS* site). 2D Gaussian fits yielded in 3D-SIM a FWHM of 151, 125 and 422 nm resolution on X, Y and Z directions respectively. These measurements are slightly higher than the PSF size obtained from beads, but this is consistent with live-cell imaging where ParB-GFP sub-clusters exhibit a confined dynamic behavior with time-scales in the order of the acquisition rate (10 ms) and lower than the overall 3D-SIM imaging time (~ 20s).

V. Resolution of 3D-PALM imaging was estimated by the distribution of single localizations within each ParB-mEos2 sub-cluster in fixed cells (HM677 strain, *parS*- $\Delta 7$, single *parS* site). Left and right panels show the X and Z distribution of localizations of a single ParB-mEos2 cluster. A Gaussian fit (green solid line) on each distribution of single molecule events belonging to a sub-cluster gave a FWHM of 25, 18 and 41 nm in X Y and Z directions, respectively. Thus, in 3D-PALM, resolution improved with respect to wide-field imaging by a factor of ~10.

Panel B: Size and number of ParB sub-clusters of origin domain.

I. To quantify the composition and sizes of ParB clusters, nucleoids were segmented and the 3D intensity of the ParB-GFP signal was independently analyzed to detect the entire ParB cluster and the sub-clusters composing it (see Figure S6a and Supplemental Experimental Procedures). Distribution in the number of ParB-GFP sub-clusters per origin ParB cluster for wild-type (red circles) and *parS*- $\Delta 7$ cells (green squares) are shown. A log-normal function (solid lines) was fitted to each distribution. In wild-type cells, ParB clusters displayed 2.8 ± 2 (mean \pm s.d.) ParB sub-clusters in average (HM671, red circles). In contrast, for a strain containing a single origin-proximal *parS*³⁵⁹ site only 1.2 ± 0.8 (mean \pm s.d.) ParB sub-clusters were detected (*parS* $\Delta 7$, HM673, green squares).

II-III. The robustness and accuracy of the clustering procedure was evaluated by measuring the distribution of the number of ParB clusters per nucleoid and of the distance between ParB clusters for wild-type and *parS*- $\Delta 7$ cells. Y-axes represent number of ParB clusters detected. (II) Distribution of the number of ParB clusters per nucleoid for wild-type (red circles) and *parS*- $\Delta 7$ cells (green squares). Distributions were fitted by a normal function (solid and dotted lines for wild-type and *parS*- $\Delta 7$, respectively). Mean number of ParB clusters per nucleoid were: 1.9 ± 0.6 (mean \pm s.d.) and 2.0 ± 0.7 (mean \pm s.d.) for wild-type and *parS*- $\Delta 7$ strains, respectively. (III) Distribution of distances between ParB clusters within the same nucleoid for wild-type (red circles) and *parS*- $\Delta 7$ cells (green squares). Means resulting from a log-normal fit were: 1500 ± 450 nm (mean \pm s.d.) and 1400 ± 500 nm (mean \pm s.d.) for wild-type and *parS*- $\Delta 7$ strains, respectively. Thus, the number of ParB clusters per nucleoid, as well as the average maximal distance between ParB clusters, was independent of the number of *parS* sites present.

IV. Distribution of the number of ParB-GFP sub-clusters per nucleoid for wild-type (red circles) and *parS-Δ7* cells (green squares). A log-normal function (solid lines) was fitted to each distribution. The number of sub-clusters per nucleoid shifted from 5.0 ± 0.2 (mean \pm s.e.m) in wild-type (strain HM671) to 2.0 ± 0.5 (mean \pm s.e.m) in the *parS-Δ7* mutant (strain HM673). These results are consistent with the number of sub-clusters per ParB cluster (panel I) and the average number of ParB clusters per cell (panel II).

Panel C: Distributions of origin ParB cluster sizes from 3D-SIM and 3D-PALM, and 2D kymographs of origin ParB cluster sizes and number of ParB-GFP sub-clusters during the cell cycle.

I. Distribution of origin ParB cluster sizes. The sizes of ParB clusters were estimated from the maximal distance separating ParB-GFP sub-clusters within each ParB cluster, computed from 3D-SIM images acquired on live, wild-type cells (strain HM671; Figure S6a). Distribution was fitted with a log-normal function (solid lines) with the resulting mean size of ParB clusters being 440 ± 210 nm (mean \pm s.d.).

II. Distribution of sizes of ParB clusters from 3D-PALM imaging of ParB-mEos2 in fixed wild-type cells (strain HM675). The procedure used to segment the cells and to cluster localizations belonging to the same origin ParB cluster are detailed in the Supplemental Experimental Procedures. The size of each ParB cluster was estimated by computing the diameter of the sphere containing 95% of the ParB-mEos2 signal belonging to that ParB cluster. Distribution was fitted with a log-normal function (solid line) with a resulting mean size of 290 ± 140 nm (mean \pm s.d.). The discrepancy with the mean cluster size obtained by 3D-PALM can be explained by several reasons: 1) the higher resolution of this approach : ~ 80 nm for 3D-PALM and 120 nm for 3D-SIM; 2) the fact that 3D-SIM is performed in live cells while 3D-PALM in fixed cells. Differences may arise from displacements of the ParB clusters occurring during the acquisition: 3D-PALM was performed in fixed cells due to the intrinsically low acquisition rate of this method (~ 1 -5 min per image); whereas 3D-SIM was performed in live cells at an acquisition speed of ~ 20 sec per volume; 3) the nature of the raw data. While in 3D-PALM we obtain localization of individually localized molecules, in 3D-SIM we obtain a 3D density (i.e. a scalar field). In 3D-SIM, we find ParB sub-clusters and then determine the maximum distance between any two sub-clusters within the same origin ParB cluster. This measurement excludes all cases where a single ParB sub-cluster is detected per ParB cluster, which in some cases represents an important proportion of cells in a population. In contrast, in 3D-PALM we estimate the size of the ParB cluster by calculating the diameter of the sphere that contains 95% of the localization events. Thus, in 3D-PALM ParB clusters with a single ParB sub-cluster will also contribute to this measurement. As these clusters are small (their size is defined often by the resolution of 3D-PALM), they will tend to lead to an over-estimation in the distribution of ParB clusters by 3D-SIM.

III,VI. Number of ParB-GFP sub-clusters per origin ParB cluster as function of the cell cycle and the ParB cluster axial position in the nucleoid (III) in wild-type cells with all naturally-occurring *parS* sites (HM671), (VI) in cells with 1 *parS* site (*parS-Δ7*, HM673).

IV,VII. Density of localizations of ParB-GFP clusters as function of the cell cycle and the ParB cluster axial position in the nucleoid (IV) in wild-type cells with all naturally-occurring *parS* sites (HM671), (VII) in cells with 1 *parS* site (*parS-Δ7*, HM673).

V,VIII. ParB cluster size as function of the cell cycle and the ParB cluster axial position in the nucleoid (V) in wild-type cells with all naturally-occurring *parS* sites (HM671), (VIII) in cells with 1 *parS* site (*parS-Δ7*, HM673).

Supplemental Movie 1. Movie of structure shown in Figure 1b.

Supplemental Movie 2. Movie of structure shown in Figure 3b.

Supplemental File *WT matrix .zip*. Hi-C matrix of Figure 1a.

Supplemental File *DeltaParS matrix .zip*. Hi-C matrix of Figure 3a.

Supplemental File *DeltaSpo0J matrix .zip*. Hi-C matrix of Figure 3a.

Supplemental File *DeltaSMC matrix .zip*. Hi-C matrix of Figure 3a.

Supplemental Experimental Procedures

Strains, media, and growth conditions

Nutrient agar (Euromedex) was used for routine selection and maintenance of *B. subtilis*. Cells were grown at 30°C in either M9 minimal media containing 0.5% glucose, 0.5% succinate and 0.1% glutamate for slow growth conditions or in Luria-Bertani (LB) medium for rapidly growing conditions.

Supplements were added as required: 0.02 mg/ml tryptophan, 40 mg/ml phenylalanine, 30 mg/ml (for single copy plasmids) or 100 mg/ml ampicillin, 5 mg/ml chloramphenicol, 2 mg/ml kanamycin, 50 mg/ml spectinomycin, and 15 mg/ml tetracycline for strain selection. Rifampicin treatment involved incubation with 25 µg/mL rifampicin for 20 minutes under gentle agitation before imaging, or before addition of formaldehyde for 3C experiments.

B. subtilis strains were derived either from the prototrophic strain PY79 (Youngman et al., 1983) or 168CA (Kunst et al., 1997). Standard techniques were used for strain construction (Harwood and Cutting, 1990). Transformation of competent *B. subtilis* cells was performed using an optimized two-step starvation procedure as previously described (Anagnostopoulos and Spizien, 1961; Hamoen, 2002). General manipulation of DNA was performed as described (Sambrook et al., 1989). All plasmids were verified by sequencing. Sequences of oligonucleotides used in this study are available upon request.

For conventional, structured illumination and super-resolution imaging (see below) proteins of interest were either tagged with monomeric GFP (Cormack et al., 1996) or photoactivatable mEos2 (McKinney et al., 2009) codon optimized for *B. subtilis*. Strains carrying the Fluorescent Repressor Operator System (FROS) with tetR/Tet-CFP or lacO/Lac-YFP pairs were built as described previously (Lau et al., 2003).

See below and Table S1 and S2 for the detailed description of all plasmids and strains used in this study.

Plasmid construction

pAK05 [*'sigX parS²⁰⁶::zeo*] was generated by ligation with a HindIII-Asp718I PCR product containing the 3' end of sigX (oAK17 + oAK18 and 168CA genomic DNA as template) and pHM457 cut with HindIII-Asp718I.

pAK09 [*'sigX parS²⁰⁶::zeo resE'*] was generated by ligation with a SacI-SacII PCR product containing the 5' end of resE (oAK15 + oAK16 and 168CA genomic DNA as template) and pAK05 cut with SacI-SacII

pAK11 [p_{pho}] was generated by subcloning a BamHI fragment (p_{pho}mycin resistant cassette) from pIC22 (Steinmetz and Richter, 1994) into pHM1.

pAK13 ['yhaX^{-parS90} p_{pho}] was generated by ligation with a SacI-SacII PCR product containing the 3' end of yhaX (mutating the parS⁹⁰ sequence found within yhaX gene while maintaining the amino acid coding sequence for the YhaX protein) (oAK38 + oAK39 and 168CA genomic DNA as template) and pAK11 cut with SacI-SacII

pAK14 [p_{pho} hemZ'] was generated by ligation with a XhoI-Asp718I PCR product containing the 5' end of hemZ (oAK40 + oAK41 and 168CA genomic DNA as template) and pAK11 cut with XhoI-Asp718I.

pAK15 ['yhaX^{-parS90} p_{pho} hemZ'] was generated by subcloning a SacI-SacII fragment ('yhaX^{-parS90}) from pAK13 into pAK14.

pAK23 ['yhaX^{-parS90} tet hemZ'] was generated by ligation with a BamHI-PstI PCR product containing the tetracycline resistant cassette (oAK47 + oAK51) from pBEST309 (Itaya., 1992 Construction of a novel tetracycline resistance gene cassette useful as a marker on the Bacillus subtilis chromosome.) to replace the p_{pho}mycin resistant cassette and pAK15 cut with BamHI-PstI.

pAK26 [bla cat 'soj-spo0J::neo yyaC'] was generated by ligation with a BlnI-NotI PCR fragment (soj-spo0J-neo) (oAK55 + oGJS431 and pHM48 as DNA template) and pHM23 cut with BlnI-NotI.

pAK28 [bla cat 'soj-Δspo0J::neo yyaC'] was generated by ligation with a BlnI-NotI PCR fragment ('soj-Δspo0J-parS-neo) (oAK55 + oGJS431 and pHM52 as DNA template) and pHM23 cut with BlnI-NotI.

pAK32 [bla cat 'soj-spo0J-parS::neo yyaC'] was generated by ligation with a SacII-XbaI PCR fragment ('soj-spo0J-parS') (oAK52/oAK53 and pHM142 as DNA template) and pAK26 SacII-XbaI.

pHM109 [P_{soj}-(soj spo0J) neo 'yyaC'] was generated by subcloning a NcoI-SacI fragment (P_{soj}-soj-spo0J neo yyaC) from pHM16 (Murray et al., 2006) into pOU82 (Larsen et al., 1984).

pHM110 [P_{soj}-(soj spo0J-gfp^{mut2})] is a derivative of pHM109 where the stop codon of spo0J was deleted, a linker encoding 17 amino acids (ELPGPELPGPELPGPEF) and ending with an EcoRI site was introduced (Glaser et al., 1997), and a PCR product containing gfp^{mut2} (oHM79 + oHM80 with AH3159 genomic DNA as template; (Real et al., 2005) was cloned downstream of spo0J using EcoRI-XbaI.

pHM142 [bla cat P_{soj}-soj-spo0J-parS::neo yyaC'] was generated by ligation with a EcoRI-HindIII PCR fragment ('spo0J-parS'-spo0J') (oHM11/oHM76 and DCL484 (Lin and Grossman, 1998) as DNA template) and pHM16 cut with EcoRI-HindIII.

pHM146 [$\text{lacO}_{\sim 150}$ cat $\text{lacO}_{\sim 150}$] was generated by subcloning an FspI-EcoRV fragment (cat) from pDG3661 (Krásný and Gourse, 2004) into pLAU43 (Lau et al., 2003).

pHM148 [$P_{\text{soj}}\text{-(soj spo0J)}$ neo $\text{tetO}_{\sim 150}$ 'yycC] was generated by subcloning an EagI fragment ($\text{tetO}_{\sim 150}$) from pLAU44 into pHM109 (Lau et al., 2003).

pHM149 [$\text{pdp lacO}_{\sim 150}$ cat $\text{lacO}_{\sim 150}$] was generated by ligation with an AflIII-NheI PCR product containing the 3' end of pdp (oHM139 + oHM140 and 168CA genomic DNA as template) and pHM146 cut with AflIII and NheI.

pHM159 [$P_{\text{soj}}\text{-(soj } \Delta\text{spo0J)}$ neo 'yycC] was generated by digesting pHM109 with StuI and HindIII (partial), filling the 5' overhang with Klenow, and then ligating together the blunt ends of the backbone.

pHM164 [$P_{\text{soj}}\text{-(soj } \Delta\text{spo0J)}$ neo $\text{tetO}_{\sim 150}$ 'yycC] was generated by subcloning an Asp718I-XbaI fragment ($P_{\text{soj}}\text{-(soj } \Delta\text{spo0J})$) from pHM159 into pHM148.

pHM355 [$P_{\text{soj}}\text{-(soj spo0J-mEos2)}$ neo 'yycC] was generated by ligation with an EcoRI-XbaI PCR product containing mEos2 (oHM296 + oHM297 and pMN_BSmEos2 as template DNA) and pHM110 cut with EcoRI and XbaI (note pHM110 was subjected to partial EcoRI digest).

pHM442 [$\text{pdp lacO}_{\sim 150}$ cat $\text{lacO}_{\sim 150}$ 'hutM] was generated by ligation with a NdeI-XbaI PCR product containing the 3' end of hutM (oHM137 + oHM138 and 168CA genomic DNA as template) and pHM149 cut with NdeI and XbaI.

pHM457 [zeo] was generated by ligation with an EcoRI PCR product containing the zeomycin resistant cassette (oHM381 + oHM382 and p7Z6 plasmid DNA as template (Lin et al., 2013) and pHM1 cut with EcoRI).

Strain construction

AK215: To construct the $\Delta 9\text{parS}$ mutant (AK205), pAK09 was integrated by double crossover into BSN1657 ($\Delta 8\text{parS}$) downstream of resE to remove parS^{206} . To construct $\Delta 10\text{parS}$ mutant (AK215), pAK23 was as integrated by double cross-over into AK205, replacing the parS^{90} sequence found within the yhaX gene (while maintaining the amino acid coding sequence for the YhaX protein).

AK241 [$\Delta\text{spo0J::neo}$] was constructed by integrating pAK28 by double crossover into PY79 that will remove the upstream sequence of spo0J while maintaining the parS sequence within spo0J.

AK243 [$\Delta 10\text{parS spo0J::neo}$] was constructed by integrating pAK32 by double crossover into AK215 to introduce the kanamycin resistance cassette downstream of spo0J.

AK487 [$\text{smc}'\Omega(\text{P}_{\text{spac}}\text{-smc erm})$] was constructed by integrating pMUTIN4- smc' by single crossover into the smc gene of PY79. The plasmid is then maintained by growing the strain with erythromycin and IPTG to induce smc expression.

HM890 [$\text{trpC2 dnaB134}^{\text{ts}}$] was constructed in two steps. First, a PCR product containing the $\text{dnaB134}^{\text{ts}}$ allele (oHM362 + oHM363 with 168ts-134 genomic DNA as template; Mendelson & Gross 1967) was co-transformed with the unstable plasmid pLOSS ($\text{spec}^r \text{lacZ}^+$; (Claessen et al., 2008)) into BS168. Transformants were selected on spectinomycin and then screened for temperature sensitivity on plates at 48°C. The DNA replication block was confirmed by staining cells with DAPI and visualizing DNA using epifluorescence microscopy. Second, a temperature sensitive clone was streaked onto X-gal and white colonies were screened for sensitivity to spectinomycin, confirming that the pLOSS plasmid had been lost.

Synchronization of B. subtilis cells

Synchronizations were performed as previously described (Su'etsugu and Errington, 2011) with minor changes. Strain HM890 (BS168 - $\text{trpC2 dnaB134}^{\text{ts}}$) was grown in LB medium at 30°C. The culture ($A_{600} \sim 0.2$) was then mixed with an equal volume of prewarmed (60°C) medium and incubated at 45°C for 2 h so that ongoing replication can terminate. The culture was then mixed with one volume of cold medium (16°C) and incubated at 30°C to release replication initiation. Aliquots from the population were sampled before release at 30°C, then at 5, 30 and 60 minutes after release, to be imaged or processed with formaldehyde.

Sample preparation for microscopy imaging

In vivo imaging

Before image acquisitions, microscopy coverslip and glass slides were rinsed with acetone and dried over an open flame to eliminate any remaining fluorescent contaminations. Next they were placed in a rack (to ensure complete cleaning from both sides of the slide) and plasma cleaned for 30 minutes using a Femto plasma cleaner (Diener electronics, Germany).

A frame of double-side adhesive tape was placed on a glass slide and a ~5mm channel was extruded from its center. 50 μl of 2 % melted agarose (diluted in M9 media, melted at 90°C) were spread on the center of the glass slide and covered with a second glass slide to ensure a flat agarose surface. The sandwiched slides were kept on a horizontal position for 5 min under external pressure at room temperature (RT) to allow the agarose to solidify. The high agarose concentration improves the stability of the pad during 3D-SIM and 3D-PALM experiments. The top slide was then carefully removed when bacteria were ready to be deposited in the agar pad (below).

Cells were harvested during the exponential phase (optical density at 600 nm: ~ 0.3). If necessary, cells were stained by adding, either simultaneously or individually, 7.5 μ l of a 0.3 μ M solution of DNA dye (DAPI, Invitrogen) to 1 ml of bacterial suspension. After five minutes of incubation in the dark, the bacterial aliquot was spun down in a bench centrifuge at RT at 4000 rpm for 4 minutes. The supernatant was then discarded and the pellet suspended in 20-30 μ l minimal media. 10 μ l of the resulting bacterial solution were pipetted onto the agar. For 3D-PALM experiments, fluorescent beads were added to the bacterial suspension prior to their deposit onto agar pads for drift correction purposes.

After deposition of bacteria, the second face of the double side tape was removed and the pad was then sealed with a clean coverslip and kept in the dark for at least five minutes to allow for regular spreading of bacteria over the surface.

The concentration of DAPI was adjusted to the minimum amount necessary to obtain high quality super-resolution images. At these concentrations, no detectable differences in nucleoid sizes or densities were observed as compared to Hbs-GFP labeling under the same growth conditions. Illumination conditions were also optimized to avoid the induction of any morphological change in the chromosome due to UV excitation.

Fixation protocol for microscopy imaging

Cells were harvested during the exponential phase (optical density at 600 nm: ~ 0.3). Final concentration of fixation agents and pH were adjusted to optimize 3D-SIM and 3D-PALM imaging conditions (4.5 % Formaldehyde, 0.02 % Glutaraldehyde 100 mM buffer phosphate pH 7.4).

Cells were incubated in the fixative solution for 10 min at RT followed by 20 min on ice. Next, bacterial aliquots were spun down in a bench centrifuge at RT at 4000 rpm for 4 minutes and the pellet suspended in 1 ml of phosphate saline buffer (PBS). This step was repeated three times and final re-suspension before imaging was in 50 μ L of PBS buffer.

3D Structured Illumination Microscopy (3D-SIM)

Instrumentation and imaging

Samples were prepared as described above and mounted on the OMX acquisition stage. 3D-SIM imaging was performed on an OMX V3 microscope (Applied Precision Inc.) equipped with an X60/1.42 oil PlanSApo objective (Olympus) and three emCCD cameras. 405 nm and 488 nm excitation lasers lines were used to excite DAPI and GFP, respectively. Dual color raw data were acquired sequentially. For each channel, a total of 255 images made of 17 different Z-planes separated by 125 nm each were acquired. Single color raw data contained 225 images for 15 Z-planes. Three different angles (-60° , 0° and $+60^\circ$) as well as five phase steps were used to reconstruct 3D-SIM images using softWoRx v5.0 (Applied Precision Inc.). Final voxel size was 39.5 nm in xy and 125 nm in z for a final 3D stack volume of $40 \times 40 \times 2 \mu\text{m}^3$. Multicolor TetraSpeck beads (100 nm in diameter, Invitrogen) were used to measure x, y and z offsets, rotation about the z-axis and magnification differences between fluorescence channels. These corrections were applied to the reconstructed images. The same beads were used to validate the reconstruction process ensuring a final resolution of ~ 120 nm in xy and ~ 300 nm in z depending on the wavelength. Acquisition parameters were used as follows: DAPI, 5-10 ms exposure with 10% transmission of the 405 nm excitation line; Hbs-GFP, 10 ms exposure with 31.3% transmission of the 488 nm excitation line.

Analysis of 3D-SIM data

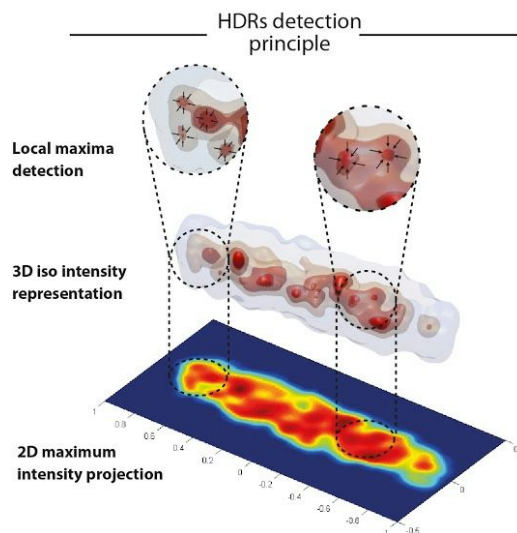
3D-SIM data were analyzed using home-made routines written in Matlab (Mathworks, Inc, US). Each individual nucleoid was automatically segmented using a 3D maximum entropy thresholding algorithm for binarization and minimum and maximum volume values for nucleoids detection. The center of mass, long and short axis were computed on the binarized nucleoids and used to rotate the original nucleoid so that the major nucleoid axis was aligned with the x-axis.

Principle of high-density chromosomal region (HDR) detection.

3D local maxima were then detected using a multi-directional derivation algorithm to detect local intensity maxima in a 3D scalar field (see Figure below). In order to minimize the effect of noise (intensity fluctuations partially due to shot noise) a criteria is set so that all voxels surrounding a local maxima need to see a gradual intensity increase over a range of 3 voxels (~ 120 nm in XY, 375 nm in Z). HDRs passing such criteria are selected and their 3D position is determined with single voxel precision (~ 39.5 nm in XY, 125 nm in Z).

Nucleoids lengths and widths were measured by determining the full width at half maximum (FWHM) in the long and short axes of the nucleoid, and used to normalize the

positions of 3D local maxima. To discard outliers from the distribution, histograms of width, height, and nucleoid mean intensities were fitted with a Gaussian function and only nucleoids included within twice the FWHM were selected for further analysis.



*Bottom image represents the maximum intensity projection along the Z axis of a nucleoid stained with DAPI in wild type *B. subtilis* (PY79). The middle plane image is a 3D representation of the same nucleoid using 4 distinct intensity iso-values color-coded from light gray to red for low to high intensities, respectively. On top, two selected areas of the nucleoid are enlarged. In these areas, higher DNA density regions (HDRs) are visible. Black arrows pointing to the center of those regions describe the gradient intensity direction used in local maxima detection.*

Parameters affecting the detectability of domains

HDRs are regions with high density of fluorophores with respect to the surrounding local fluorescence signal, and therefore represent regions where DNA is more highly condensed. This higher degree of condensation may be related to several factors, including local density fluctuations or the coalescence of one or more CIDs. The lack of genomic specificity in this labeling method, however, does not permit us to identify individual CIDs, except for the origin domain for which the specific ParB-GFP labeling is used (see Figure 6).

Several parameters impact the detection of CIDs by single-cell imaging approaches: genomic specificity, optical resolution, the intrinsic size of CIDs, and their spatial separation with respect to other CIDs. For instance, small domains (genetically speaking) may not contain a high enough density of fluorophores to be distinguished above background. In addition, domains that are large enough to produce a detectable signal above background still have to be located at a distance from each other larger than the optical resolution of the microscope (~100-120 nm

in our experiments, see Figure S6a) to be resolved, as they would otherwise be detected as a single domain. In brief, a one-to-one correlation between CIDs detected in microscopy and Hi-C requires the labeling of entire CIDs with genomic specificity and the use of a higher-resolution microscopy method when CIDs are close together.

HDR histograms and kymographs

A kernel density estimator was used to plot the number of detected 3D local maxima (assimilated as HDRs) versus nucleoids length for each cell line used in this work. 2D histograms of the positions of the HDRs in the nucleoids were constructed as follows: nucleoids lengths were segmented into windows (typically of 250 nm) for which the mean and the standard deviation (STD) of the number of HDRs are computed, another selection was then performed to keep only nucleoids that showed a number of HDRs falling within one standard deviation of the mean. For each window, the selected nucleoids were resampled 100 times using a bootstrapping method and HDRs positions orientation were randomized along the long and short axis of the nucleoids before computing 2D histograms. The mean and STD were then calculated for each window from the 100 smoothed histograms built from the 100 bootstrapped samples.

Kymographs were computed following the same procedure but using a 100 nm running window with 20 nm steps. ParB-GFP kymographs were computed by integrating all maxima localizations within -0.5 to 0.5 over the short axis while HDRs detected by full chromosome labeling (either Hbs-GFP or DAPI staining) were integrated between -0.1 to 0.1 (unless specified otherwise).

Detection of ParB-GFP sub-clusters was performed using the same 3D local maxima detection algorithm. Only sub-clusters with a large intensity with respect to background were selected for further analysis. The threshold used was defined as follows: the histogram of 3D local maxima intensities for cells with a single *parS*³⁵⁹ (HM673) was plotted and showed two peaked and separable distributions; the low intensity distribution was due to shot noise whereas the high intensity distribution corresponded to real ParB-GFP clusters; a threshold was selected to segment these two populations. To verify the validity of this threshold, histograms of the number of ParB-GFP sub-clusters per cell and of the distance between sub-clusters were built. These distributions reflected the total number of origins in a population of cells growing in minimal medium (2 origins per cell in average, see Figure S6b, II), and the correct maximal distance between sub-clusters (~1400 nm, see Figure S6b, III). The positions of ParB-GFP sub-clusters were normalized by the length and width of the nucleoid they belonged to. To determine which sub-clusters belonged to individual origin ParB clusters, the sub-cluster positions were clustered using a cutoff distance of 500 nm, determined by computing a hierarchical cluster tree. The performance of this clustering procedure was assessed by

verifying that the number of detected origin ParB clusters and their relative distance were indistinguishable between parS³⁵⁹ (HM673) and the wild-type ParB-GFP strain (HM671) (see Figures S6b, II and III).

3D Photo-activated localization microscopy (3D-PALM)

Instrumentation and imaging

3D-PALM imaging was performed in a modified Nikon Eclipse Ti-S inverted microscope equipped with a 100x Plan-Apo Lambda oil-immersion objective (NA = 1.45) equipped with two lasers (excitation wavelengths of 405nm and 561 nm) and an active feedback autofocus system as described previously (Cattoni et al., 2013; Fiche et al., 2013). Acquisition software controlling lasers, filter wheels and camera were homemade using LabView 2012 (National InstrumentsTM). To obtain 3D imaging conditions, a corrective MicAO 3D-SR system (Imagine OpticTM, France) was inserted into the emission pathway between the microscope and the EMCCD camera (Andor Ixon 897, Ireland). The MicAO 3DSR adaptive optics device uses its deformable mirror to correct for the optical aberrations introduced in the imaging path, optimizing the photon budget and maximizing the lateral resolution for PALM experiment. For 3D detection, subtle changes in astigmatism are further added in order to axially shape the point-spread function (PSF), allowing 3D-PALM imaging with an axial resolution up to 20nm over approximately 1 μ m (~ the thickness of a bacterium). Coverslip (Marienfeld, #1.5H) were thoroughly cleaned to prevent non-specific single-molecule fluorescent detections during 3D-PALM acquisition.

3D-PALM imaging of ParB-mEos2 in fixed cells was performed by continuously acquiring between 1-2.5 10^4 images at 20Hz (50ms per frame) under continuous illumination with the 561 nm read-out laser (Sapphire 561LP, 150mW, Coherent) and 405 nm for photo-activation (StradusTM 405-100, Vortran). The read-out laser intensity used for 3D-PALM experiments was 1.2kW/cm² at the sample plane. For the activation laser (405nm), the maximum power used for photo-activating mEos2 was 0.1W/cm². The intensity of the 405nm laser was modified during the course of the experiment to maintain the density of activated fluorophores constant while ensuring that only one protein was activated at a time in a single diffraction-limited spot. Acquisition was carried out until all mEos2 proteins were photo-activated and bleached. Fluorescent beads (TetraSpeckTM, life technologies) were used as fiducial marks to correct for sample drift during post-processing analysis.

3D-PALM image analysis and rendering

Unless stated otherwise, all homemade software and routines were developed in Matlab. 3D single-molecule localizations were obtained by using Rapid STORM (Wolter et al., 2012). For each sample, the calibration curves were generated by imaging a single 100nm

TetraSpeck bead while scanning the sample stage along the optical axis (z) by steps of 50nm. For each position, the PSF was fitted with an elliptical Gaussian function and the x-y widths (w_x and w_y) were calculated in order to produce the calibration curves $w_x(z)$ and $w_y(z)$.

Localization coordinates were further processed using PALMcb, a home-made software written in Matlab. Fluorescent beads were used to correct for drift in all three directions: on agar pad, lateral and axial drifts were corrected with 10 ± 5 nm and 25 ± 10 nm precisions, respectively. Samples with abnormal drift or lesser drift precision correction were discarded.

Detection of ParB-mEos2 sub-clusters was performed as follows. Bacteria were first manually segmented using bright field images using MicrobeTracker (Sliusarenko et al., 2011). For each cell, a binarized 3D density map was computed by dividing the volume into voxels of 30nm along the x- and y-axis and 50nm along the z-axis. These values were chosen according to the lateral and axial resolution previously reported for 3D-PALM experiments based on astigmatism detection. The value of the voxels containing at least one single-molecule fluorescent event was set to 1. The value of all the other voxels were set to 0. Using the binary density map and a clustering algorithm (Cattoni et al. 2013), a list of clusters was produced and the number of fluorescent events associated to each cluster was calculated. Sub-clusters containing less than 5 detections were rejected to avoid non-specific localization events and mis-localizations artifacts.

To determine which ParB-mEos2 sub-clusters belonged to single origin domain, neighboring sub-clusters were pooled as a function of their centroid-to-centroid distance $dc-c$. When $dc-c$ was below a pre-defined threshold (usually between 300 and 500 nm), sub-clusters were merged together into the same origin ParB cluster. To ensure that sub-clusters were not associated to isolated single-molecule ParB-mEos2 molecules, only sub-clusters containing more than 30 fluorescent events were considered for further analysis.

The size of each origin ParB cluster was finally estimated by calculating the radius of the sphere centered on the ParB cluster centroid and containing 90% of the fluorescent events. For each strain, histograms of ParB cluster sizes were built by using a 25 nm binning step and weighted by the number of events within the ParB cluster. The size distribution was then fitted using a log normal probability law distribution.

Tracking of single FROS tags

For two-color FROS experiments, we used a homemade epifluorescence setup (Zeiss Axiovert 200 inverted microscope equipped with an alpha Plan-Fluar 100/1.45 NA objective; Zeiss, Le Peck, France). The 454 and 488 nm laser lines of an Argon ion laser (Spectra physics, 163-C12, Santa Clara, USA) were used to excite and monitor CFP and YFP, respectively. Fluorescence signal was collected through the same objective and passed through a filter cube containing a dichroic mirror and a dual band filter transmitting the 457 and

514 nm bands (Chroma, Vermont, USA) and imaged onto an EM-CCD camera (Andor iXon, Ultra 897, Belfast, Ireland). Laser power and intensity were controlled by an acousto-optic tunable filter. The camera exposure time used was 50 ms with a gain of 200. Alternated imaging of CFP and YFP was achieved by using alternating laser excitations (Kapanidis et al., 2005), a technology that abolishes cross-talk between emission channels. Movies of 1000 frames were acquired and individual spots were localized in each frame using multiple-trace tracker (Sergé et al., 2008). The positions identified in each channel were then clustered and associated to the closest cluster in the other channel. From those clusters hundreds of inter-foci distances are calculated and cumulated into histograms.

Chromosome conformation capture with next generation sequencing

Construction of 3C libraries (see Table S3)

3C libraries were built as previously described with minor changes (Le et al., 2013). Briefly, cells were grown in 100 ml of LB medium (final concentration: 10^6 cells/ml) at 30°C until a final concentration of $\sim 1-2 \times 10^7$ cells/ml. Cells were then crosslinked using fresh formaldehyde for 30 minutes at RT (3% final concentration; Sigma Aldrich Formalin 37%) followed by 30 minutes at 4°C. Formaldehyde was quenched with a final concentration of 0.25 M glycine for 5 minutes at RT followed by 15 minutes at 4°C. Fixed cells were pooled as 1×10^9 aliquots, collected by centrifugation, frozen in dry ice and stored at -80°C.

Frozen pellets of $\sim 1 \times 10^9$ cells were defrosted on ice and suspended in a final volume of 650 μ l 1X TE pH 8 before adding 4 μ l of ready-lyze lysozyme (35 U/ μ l; Tebu Bio), and incubated at RT for 20 minutes. SDS was added to a final concentration of 0.5% followed by 10 min RT incubation. 50 μ l of lysed cells were put in 8 tubes containing 450 μ l of digestion mix (1X NEB 1 buffer, 1% triton X-100, and 100U HpaII enzyme [NEB; C[^]CGG]) and incubated for 3 hours at 37°C. The insoluble fraction of the sample was recovered through a centrifugation step (20 min, 16000 x g; (Gavrilov et al., 2013). Pellets were then suspended in total volume of 2 mL of water, split in 4 aliquots, and diluted into 8 ml ligation buffer (1X ligation buffer NEB without ATP, 1 mM ATP, 0.1 mg/ml BSA, 125 Units of T4 DNA ligase [Fermentas 5 U/ μ l]). Ligation was performed at 16°C for 4 hours followed by a decrosslinking step consisting in an overnight (ON) incubation at 65°C in presence of 250 μ g/ml proteinase K in 6.2 mM EDTA. DNA was then precipitated with 800 μ l of 3 M Na-Acetate (pH 5.2) and 8 ml iso-propanol. After one hour at -80°C, the DNA was pelleted by centrifugation. Pellets were suspended in 500 μ l 1X TE buffer and RNA degraded with a final concentration of 0.03 mg/ml RNase A and incubated for one hour at 37°C. DNA was transferred into 2 ml centrifuge tubes, extracted twice with 500 μ l phenol-chloroform pH 8.0, precipitated, washed with 1 ml cold ethanol 70% and diluted in 30 μ l 1X TE buffer. All tubes were pooled and the resulting 3C library was quantified on gel using QuantityOne software (BioRad).

Construction of HiC libraries

For several libraries (see Table S3), a biotin enrichment step was included after digestion in the above protocol, similar to the one presented in the Hi-C protocol (Lieberman-Aiden et al., 2009). After the 3 hours digestion, the samples were centrifuged at 16000 x g for 20 minutes and the insoluble fraction of chromatin was recovered. Each pellet was then suspended in 100 μ l of restriction buffer 1X (NEBuffer 1 for HpaII or NEBuffer 2 for HindIII) (New England Biolabs). The digested extremities were decorated with biotin by repairing the restriction sites overhangs with a mix of dGTP, dTTP and dATP (10 mM each – Life Technologies) and biotin-14-dCTP (10 mM; Metkinen chemistry, Finland) incubated with

Klenow Large fragment (3 μL x 5000 units/mL; 5 μL water; 1 μL 10X NEBuffer 2 [NEB]). Samples were incubated at 25°C for 45 minutes. Ligation and further steps were done as described for the 3C protocol except that 250 U of T4 ligase were used in place of 125 U for the ligation step.

Processing of libraries for Illumina sequencing

Aliquots of 5 μg of each 3C library were dissolved in water (final volume 130 μL) and sheared using a Covaris S220 (Duty cycle 5, Intensity 5, cycles/burst 200, time 60 sec for 4 cycles). The DNA was purified on QIAquick column and processed into a pair-end library using the Illumina Paired-End DNA sample Prep Kit (Illumina – PE-930-1001). Ligation of custom-made adapters (Table S4) was performed on ~ 8 μg of the 3C library at RT for 3h (30 μL final; 1X ligation buffer NEB, 1200 Units of T4 DNA ligase [NEB 400 U/ μL]) followed by a 20 min incubation at 65°C.

DNA fragments ranging in size from 400 to 800 bp were purified using a PippinPrep apparatus (SAGE Science). For the Hi-C libraries, each sample was enriched at this step as described (Lieberman-aiden et al., 2009). For each library, several PCR reactions were performed on 1, 2 or 3 μL of the collected DNA to determine the optimal parameters to amplify the library for sequencing (Illumina primers PE1.0 and PE2.0; Phusion Taq polymerase [Finnzymes]). The PCR parameters were as follows: (1) 30 sec at 98°C, (2) 9, 12 or 15 cycles x [10 sec at 98°C; 30 sec at 65; 30 sec at 72°C], (3) 7 minutes at 72°C. 25 μL of each reaction was run on agarose gel and stained with ethidium bromide in order to determine the optimal amount of template and number of cycles. Eight independent PCR reactions were then performed using the optimal protocol, whose products were purified on Qiagen MinElute columns and pair-end sequenced on an Illumina platform (HiSeq2000, HiSeq2500 or NextSeq).

Processing of PE reads

Sequencing data for each library was demultiplexed using the corresponding tags present on the custom-made adapter and processed as follows: First, PCR amplification duplicates, identified from sharing identical 6 nucleotide sequences at the 6Ns position present on each adapter, were discarded. Each read of a pair was then aligned independently using Bowtie 2 in its most sensitive mode (Langmead and Salzberg, 2012). We used an iterative alignment procedure similar to Imakaev (Imakaev et al., 2012), i.e. only the first 20 base pairs of the read were initially mapped then the length of the read was progressively increased until the mapping became unambiguous, with a mapping quality above 40).

Generation of 3C contact maps

Each mapped read was assigned to a restriction fragment. Pairs of reads separated by less than 5 restriction sites were discarded from the analysis, since they correspond most likely to looping events of undigested DNA molecules, and as described in Cournac et al. (Cournac et al., 2012) (see also (Jin et al., 2013)). Because these restriction fragments present a large heterogeneity in sizes, we chose to bin the genomes into regular units (or bins) of 2 kb segments, that were eventually, and depending on the analysis, pooled together into larger bins (contact maps presented in the article are all made with 4kb bins). Bins corresponding to repeated elements such as the highly conserved clusters of rRNA genes present a coverage deficit as a result of the impossibility to align the reads unambiguously against these sequences, and the corresponding vectors were set to 0. In addition, the important GC% variations found on prophage sequences and horizontally transferred genes present in the BS168 genome disturb the number of restriction fragment per bin. The contact map was normalized using the sequential component normalization procedure (SCN) described in (Cournac et al., 2012), a treatment similar to the iterative normalization procedure described in (Imakaev et al., 2012). The SCN procedure ensures that the sum over the column and lines of the matrix equals 1, which compensate for the heterogeneity in the various restriction fragments and therefore reduces the biases inherent to the protocol. Raw contact maps centered on the *ori* region for WT, mutants (*parS*, *parB*, SMC) and cell cycle (G1, +5', +60') are provided in the supplementary material as zipped .txt files (with either 2 or 4 kb bins).

Identification of domains frontiers using directional index

To quantify the degree of directional preference for a given bin, we applied on correlation matrices a procedure very similar to the one used in Le et al. (2013). More precisely, for each 10 kb bin, we extracted the vector of interactions from the correlation matrix between that bin and bins at regular 10 kb intervals, up to 100 kb in both left and right directions. We then compared the two vectors with a paired t-test to assess whether the strength of interactions remain significantly stronger in one direction compared to the other. A value of 0.05 was used as a threshold to assess a statistical significant difference. The directional preferences for the bin along the chromosome are represented as a bar plot with positive and negative t-values shown as red and green bars, respectively (Le et al., 2013). The bars of the bins with t values below -2 or above 2 (corresponding to a p-value = 0.05) were trimmed for clarity of presentation. Between two domains identify in the contact matrixes (CID in Le et al., 2013), the directional preference of bins changed dramatically, as illustrated by alternating red and green colors (Le et al., 2013).

Circos plot

Circos plot was used to obtain a circular representation of the inter-arms contacts obtained from Hi-C contact map (Krzywinski, 2009). Only the quarter of the contact matrix containing the secondary diagonal was considered to favor contacts between left and right arms (see panel below). To consider only the most frequent interactions and remove background the resulting contact map frequencies were rescaled from 0 to 1 and only contact frequencies above 24% were selected. Grey lines in Figure 2c represent a fraction (1000) of the total inter-arm contacts detected using this procedure (54816). Contacts connecting two SMC-ScpAB enriched regions were colored in red. Contacts originating in an SMC-ScpAB enriched site but ending in a site with no enrichment were showed in black. Each SMC-ScpAB specific contact was obtained by averaging neighboring regions to reduce noise. Note that over 70% of all SMC-ScpAB-enriched inter-arm contacts bridge SMC-ScpAB binding regions of both replichores (percentage estimated as $100 * N_{\text{red contacts}} / (N_{\text{red contacts}} + N_{\text{black contacts}})$).

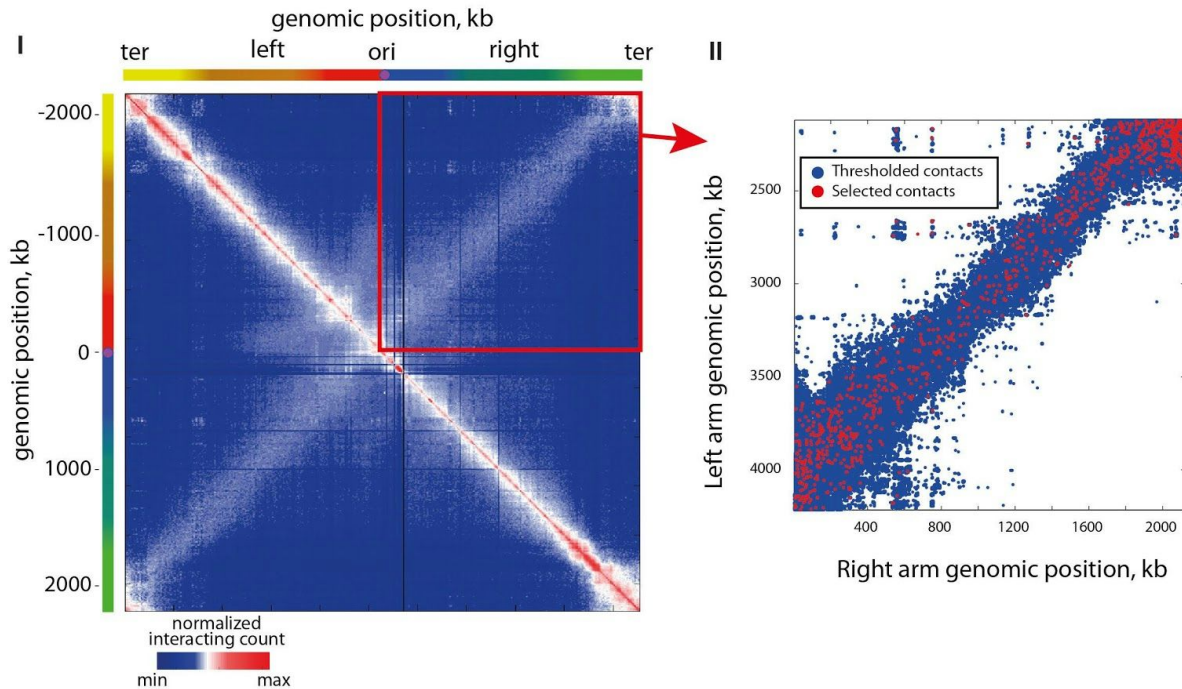


Illustration of the contacts exploited to generate the circos representation

Following replication progression using HiC reads

The progression of DNA replication was followed using the reads directly from the corresponding libraries (Table S3 and Figure S2, panel III). Reads were mapped against reference genomes using Bowtie, then quantified for every 1 Kb segment and normalized to the

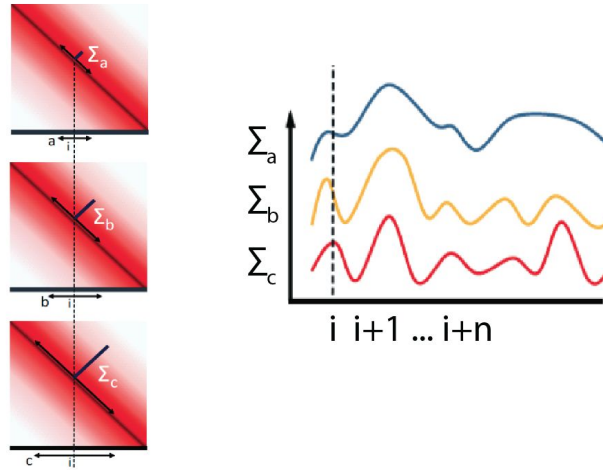
total number of successfully-mapped reads. Finally, we computed the Number of Reads Per Kb per million mapped reads (RPKM).

Multi-scale domainograms

The values $D(p,s)$ of the domainogram D at genome position p and scale s were computed as follows from the normalized Hi-C matrix M . First, we computed the Pearson correlation matrix C from M using the `corrcoef` matlab built-in function. $D(p,s)$ was then computed from C :

$$D(p,s) = \sum_{i=1}^s C(p+i, p-i)$$

, where D was normalized so that the minimum and maximum values for each scale s were respectively set to 0 and 1. The following figure describes in more detail the procedure used to build domainograms.



Domainograms were built from a given contact map follows. For each position (bin) i along the genome, windows of sizes a , b , c , etc., centered on i , were defined. For each size, the sum of the perpendicular to the main diagonal was computed for each i position and plotted (bottom).

This process was performed over the entire genome and over a broad distribution of window sizes. The two-dimensional pattern appearing reflects the organization of the chromosome at multiple scales.

3D topological representations of the *B. subtilis* chromosome

The reconstruction of 3D structures from SCN normalized (Cournac et al., 2012) Hi-C matrix was performed using ShReC3D (Lesne et al., 2014).

Table S1*Bacterial strains employed in this study*

Strain	Parent Strain	Genotype	Reference
168CA	BS168	wild-type	(Kunst et al., 1997)
168ts-134	BS168	indole- thymine- dnaB134 ^{ts}	Mendelson & Gross (1967)
Bs138	168CA	trpC2 Ω amyE::cat neo)(P _{hbs} -hbs-gfp)	(Leaver et al., 2009)
BSN1657	PY79	Δ 8parS	(Sullivan et al., 2009)
AK205	PY79	Δ 9parS	This work
AK215	PY79	Δ 10parS	This work
AK241	PY79	Δ spo0J::neo	This work
AK243	PY79	Δ 10parS spo0J::neo	This work
AK359	168CA	trpC2 thr::mls(P _{pen} -lacI Δ 11-cfp) hutM::cat(lacO _{~300}) cgeD::tet(P _{pen(mutTTAG)} -tetR-yfp) (Δ spo0J tetO _{~150})::neo	This work
AK487	PY79	smc' Ω (P _{spac} -smc erm)	This work
AK525	168CA	trpC2 Δ spo0J::neo amyE::cat(P _{hbs} -hbs-gfp)	This work
HM671	PY79	spo0J-gfp::neo	This work
HM673	PY79	spo0J-gfp::neo Δ 7parS	This work
HM675	PY79	spo0J-mEos2::neo	This work
HM677	PY79	spo0J-mEos2::neo Δ 7parS	This work
HM890	168CA	trpC2 dnaB134 ^{ts}	This work
HM892	168CA	thr::mls(P _{pen} -lacI Δ 11-cfp) hutM::cat(lacO _{~300})	This work
HM923	168CA	trpC2 thr::mls(P _{pen} -lacI Δ 11-cfp) hutM::cat(lacO _{~300}) cgeD::tet(P _{pen(mutTTAG)} -tetR-yfp) (spo0J tetO _{~150})::neo	This work
HM1320	168CA	trpC2 amyE::cat neo)(P _{hbs} -hbs-gfp)	This work
JWV042	168CA	trpC2 amyE::neo(P _{hbs} -hbs-gfp)	(Leaver et al., 2009)

KPL682	JH642	trpC2 pheA1 thr::mls(P _{pen} -lacIΔ11-cfp)	(Lemon and Grossman, 2000)
PY79 (HM 255)	BS168	wild-type	Youngman et al. 1983
BWX925	PY79	yycR(-7°)::tetO48 (cat), pelB(+174°)::lacO48 (kan), ycgO::PftsW tetR-cfp (spec) terminators PftsW lacI-mypet, dnaB134 (ts) - zhb83::Tn917 (erm)	Wang et al. 2014
BWX1206	PY79	spolIIE36, yrvN(-120°)::lacO48 (phleo), ykoW(+120°)::tetO48 (cat), ycgO::PftsW tetR-cfp (spec) terminators PftsW lacI-mypet	Wang et al. 2014
BWX1053	PY79	yuxG(-87°)::lacO48 (phleo), yhdG(+87°)::tetO48 (cat), ycgO::PftsW tetR-cfp(kan) terminators PftsW lacI-mypet	Wang et al. 2014

Table S2*Plasmids employed in this study*

Plasmid	Genotype	Reference
pAK05	bla cat 'sigX Δ parS ²⁰⁶ ::zeo	this work
pAK09	bla cat 'sigX Δ parS ²⁰⁶ ::zeo resE'	this work
pAK11	bla cat pheo	this work
pAK13	bla cat 'yhaX ^{-parS90} pheo	this work
pAK14	bla cat pheo hemZ'	this work
pAK15	bla cat 'yhaX ^{-parS90} ::pheo hemZ'	this work
pAK23	bla cat 'yhaX ^{-parS90} ::tet hemZ'	this work
pAK26	bla cat 'soj-spo0J::neo yyaC'	This work
pAK28	bla cat 'soj- Δ spo0J::neo yyaC'	This work
pAK32	bla cat 'soj-spo0J-parS::neo yyaC'	This work
pHM1	bla cat	(Murray et al., 2006)
pHM16	bla cat P _{soj} -soj-spo0J::neo yyaC'	(Murray et al., 2006)
pHM23	bla cat 'yyaB-P _{soj} -gfp-soj-spo0J::neo yyaC'	(Murray and Errington, 2008)
pHM48	bla cat P _{soj} -soj-spo0J::neo yyaC'	(Murray and Errington, 2008)
pHM52	bla cat P _{soj} -soj- Δ spo0J::neo yyaC'	(Murray and Errington, 2008)
pHM109	bla P _{soj} -(soj spo0J) neo 'yyaC	this work
pHM110	bla P _{soj} -(soj spo0J-gfp ^{mut2})	this work
pHM142	Bla cat P _{soj} -soj-spo0J-parS::neo yyaC'	This work
pHM146	bla lacO _{~150} cat lacO _{~150}	this work
pHM148	bla P _{soj} -(soj spo0J) neo tetO _{~150} 'yyaC	this work
pHM149	bla 'pdp lacO _{~150} cat lacO _{~150}	this work
pHM159	bla P _{soj} -(soj Δ spo0J) neo 'yyaC	this work
pHM164	bla P _{soj} -(soj Δ spo0J) neo tetO _{~150} 'yyaC	this work
pHM355	bla P _{soj} -(soj spo0J-mEos2) neo 'yyaC	this work
pHM442	bla 'pdp lacO _{~150} cat lacO _{~150} 'hutM	this work
pHM457	bla cat zeo	this work
pMUTIN4-smc'	bla erm P _{spac} -smc' lacZ lacI	gift from J. Errington

Table S3*Hi-C datasets*

Strain	Cell cycle stage	Growth medium	Protocol	Sequencing adapters	Number of long range interactions
PY79	Asynchronous	LB	3C	78/79	996 446
PY79	Asynchronous	MM	3C	108/109	1 419 439
HM1320	Asynchronous	LB	3C	70/71	11 708 428
HM1320	Asynchronous	MM	3C	174/175	8 554 746
HM1320	Transcription inhibited	LB	3C	72/73	2 317 643
AK215	Asynchronous	LB	3C	108/109	1 565 171
AK215	Asynchronous	MM	3C	110/111	7 000 424
AK241	Asynchronous	LB	3C	106/107	7 177 511
AK487	Asynchronous	LB	3C	70/71	13 037 890
AK487	Asynchronous	MM	3C	70/71	3 189 783
HM890	G1	LB	Hi-C	110/111	3 455 530
HM890	G1 + 5 min	LB	Hi-C	78/79	15 164 844
HM890	G1 + 30 min	LB	Hi-C	70/71	2 722 389
HM890	G1 + 60 min	LB	Hi-C	164/165	9 512 934

Table S4*List of the custom-made Illumina adapters used in this study*

Oligos	Sequences
MM70	GTANNNNNNAGATCGGAAGAGCGGTTCAGCAGGAATGCCGAG
MM71	ACACTCTTTCCCTACACGACGCTCTTCCGATCTNNNNNNNTACT
MM72	GCTNNNNNNNAGATCGGAAGAGCGGTTCAGCAGGAATGCCGAG
MM73	ACACTCTTTCCCTACACGACGCTCTTCCGATCTNNNNNNNAGCT
MM78	AGTNNNNNNNAGATCGGAAGAGCGGTTCAGCAGGAATGCCGAG
MM79	ACACTCTTTCCCTACACGACGCTCTTCCGATCTNNNNNNNACTT
MM106	TGGNNNNNNNAGATCGGAAGAGCGGTTCAGCAGGAATGCCGAG
MM107	ACACTCTTTCCCTACACGACGCTCTTCCGATCTNNNNNNNCCAT
MM108	CCANNNNNNNAGATCGGAAGAGCGGTTCAGCAGGAATGCCGAG
MM109	ACACTCTTTCCCTACACGACGCTCTTCCGATCTNNNNNNNTGGT
MM110	GTGNNNNNNNAGATCGGAAGAGCGGTTCAGCAGGAATGCCGAG
MM111	ACACTCTTTCCCTACACGACGCTCTTCCGATCTNNNNNNNCACT
MM160	GACNNNNNNNAGATCGGAAGAGCGGTTCAGCAGGAATGCCGAG
MM161	ACACTCTTTCCCTACACGACGCTCTTCCGATCTNNNNNNNGTCT
MM164	CACNNNNNNNAGATCGGAAGAGCGGTTCAGCAGGAATGCCGAG
MM165	ACACTCTTTCCCTACACGACGCTCTTCCGATCTNNNNNNNGTGT
MM174	ACGNNNNNNNAGATCGGAAGAGCGGTTCAGCAGGAATGCCGAG
MM175	ACACTCTTTCCCTACACGACGCTCTTCCGATCTNNNNNNNCGTT
MM176	TCGNNNNNNNAGATCGGAAGAGCGGTTCAGCAGGAATGCCGAG
MM177	ACACTCTTTCCCTACACGACGCTCTTCCGATCTNNNNNNNCGAT
MM178	GCGNNNNNNNAGATCGGAAGAGCGGTTCAGCAGGAATGCCGAG
MM179	ACACTCTTTCCCTACACGACGCTCTTCCGATCTNNNNNNNCGCT
MM186	CGTNNNNNNNAGATCGGAAGAGCGGTTCAGCAGGAATGCCGAG
MM187	ACACTCTTTCCCTACACGACGCTCTTCCGATCTNNNNNNNACGT

References

- Anagnostopoulos, C., and Spizien, J. (1961). Requirements for transformation in *Bacillus subtilis*. *J Bacteriol.* 81(5), 741–746.
- Barbe, V., Cruveiller, S., Kunst, F., Lenoble, P., Meurice, G., Sekowska, A., Vallenet, D., Wang, T., Moszer, I., Médigue, C., et al. (2009). From a consortium sequence to a unified sequence: the *Bacillus subtilis* 168 reference genome a decade later. *Microbiology* 155, 1758–1775.
- Berkmen, M.B., and Grossman, A.D. (2006). Spatial and temporal organization of the *Bacillus subtilis* replication cycle. *Mol. Microbiol.* 62, 57–71.
- Berlatzky, I.A., Rouvinski, A., and Ben-Yehuda, S. (2008). Spatial organization of a replicating bacterial chromosome. *Proc. Natl. Acad. Sci. U.S.A.* 105, 14136–14140.
- Cattoni, D.I., Fiche, J.-B., Valeri, A., Mignot, T., and Nöllmann, M. (2013). Super-resolution imaging of bacteria in a microfluidics device. *PLoS One* 8, e76268.
- Claessen, D., Emmins, R., Hamoen, L.W., Daniel, R.A., Errington, J., and Edwards, D.H. (2008). Control of the cell elongation-division cycle by shuttling of PBP1 protein in *Bacillus subtilis*. *Mol. Microbiol.* 68, 1029–1046.
- Cormack, B.P., Valdivia, R.H., and Falkow, S. (1996). FACS-optimized mutants of the green fluorescent protein (GFP). *Gene* 173, 33–38.
- Cournac, A., Marie-Nelly, H., Marbouty, M., Koszul, R., and Mozziconacci, J. (2012). Normalization of a chromosomal contact map. *BMC Genomics* 13, 436.
- Fiche, J.-B., Cattoni, D.I., Diekmann, N., Langerak, J.M., Clerte, C., Royer, C. a, Margeat, E., Doan, T., and Nöllmann, M. (2013). Recruitment, assembly, and molecular architecture of the SpoIIIE DNA pump revealed by superresolution microscopy. *PLoS Biol.* 11, e1001557.
- Fisher, J.K., Bourniquel, A., Witz, G., Weiner, B., Prentiss, M., and Kleckner, N. (2013). Four-dimensional imaging of *E. coli* nucleoid organization and dynamics in living cells. *Cell* 153, 882–895.
- Gavrilov, A.A., Gushchanskaya, E.S., Strelkova, O., Zhironkina, O., Kireev, I.I., Iarovaia, O. V, and Razin, S. V (2013). Disclosure of a structural milieu for the proximity ligation reveals the elusive nature of an active chromatin hub. *Nucleic Acids Res.* 41, 3563–3575.
- Glaser, P., Sharpe, M.E., Raether, B., Perego, M., Ohlsen, K., and Errington, J. (1997). Dynamic, mitotic-like behavior of a bacterial protein required for accurate chromosome partitioning. *Genes Dev.* 11, 1160–1168.
- Hamoen, L.W. (2002). Improving the predictive value of the competence transcription factor (ComK) binding site in *Bacillus subtilis* using a genomic approach. *Nucleic Acids Res.* 30, 5517–5528.
- Harwood, C.R., and Cutting, S.M. (1990). *Molecular Biological Methods for Bacillus* (New York: Wiley).
- Hadizadeh Yazdi, N., Guet, C.C., Johnson, R.C., and Marko, J.F. (2012). Variation of the folding and dynamics of the *Escherichia coli* chromosome with growth conditions. *Mol. Microbiol.* 86, 1318–1333.
- Imakaev, M., Fudenberg, G., McCord, R.P., Naumova, N., Goloborodko, A., Lajoie, B.R., Dekker, J., and Mirny, L.A. (2012). Iterative correction of Hi-C data reveals hallmarks of chromosome organization. *Nat. Methods* 9, 999–1003.

- Jin, F., Li, Y., Dixon, J.R., Selvaraj, S., Ye, Z., Lee, A.Y., Yen, C.-A., Schmitt, A.D., Espinoza, C.A., and Ren, B. (2013). A high-resolution map of the three-dimensional chromatin interactome in human cells. *Nature* 503, 290–294.
- Kapanidis, A.N., Laurence, T.A., Lee, N.K., Margeat, E., Kong, X., and Weiss, S. (2005). Alternating-laser excitation of single molecules. *Acc. Chem. Res.* 38, 523–533.
- Krásný, L., and Gourse, R.L. (2004). An alternative strategy for bacterial ribosome synthesis: *Bacillus subtilis* rRNA transcription regulation. *EMBO J.* 23, 4473–4483.
- Krzywinski, M., Schein, J., Birol, I., Connors, J., Gascoyne, R., Horsman, D., Jones, S.J., and Marra, M.A. (2009). Circos: an information aesthetic for comparative genomics. *Genome Res.* 19, 1639–1645.
- Kunst, F., Ogasawara, N., Moszer, I., Albertini, a M., Alloni, G., Azevedo, V., Bertero, M.G., Bessi res, P., Bolotin, a, Borchert, S., et al. (1997). The complete genome sequence of the gram-positive bacterium *Bacillus subtilis*. *Nature* 390, 249–256.
- Langmead, B., and Salzberg, S.L. (2012). Fast gapped-read alignment with Bowtie 2. *Nat. Methods* 9, 357–359.
- Larsen, J.E.L., Gerdes, K., Light, J., and Molin, S. (1984). Low-copy-number plasmid-cloning vectors amplifiable by derepression of an inserted foreign promoter. *Gene* 28, 45–54.
- Lau, I.F., Filipe, S.R., S balle, B.,  ksCID, O.-A., Barre, F.-X., and Sherratt, D.J. (2003). Spatial and temporal organization of replicating *Escherichia coli* chromosomes. *Mol. Microbiol.* 49, 731–743.
- Le, T.B.K., Imakaev, M. V, Mirny, L. a, and Laub, M.T. (2013). High-resolution mapping of the spatial organization of a bacterial chromosome. *Science* 342, 731–734.
- Leaver, M., Dom nguez-Cuevas, P., Coxhead, J.M., Daniel, R.A., and Errington, J. (2009). Life without a wall or division machine in *Bacillus subtilis*. *Nature* 457, 849–853.
- Lemon, K.P., and Grossman, A.D. (2000). Movement of replicating DNA through a stationary replisome. *Mol. Cell* 6, 1321–1330.
- Lesne, A., Riposo, J., Roger, P., Cournac, A., and Mozziconacci, J. (2014). 3D genome reconstruction from chromosomal contacts. *Nat. Methods* 11, 1141–1143.
- Lieberman-aiden, E., Berkum, N.L. Van, Williams, L., Ragoczy, T., Telling, A., Amit, I., Lajoie, B.R., Peter, J., Dorschner, M.O., Sandstrom, R., et al. (2009). Comprehensive mapping of long range interactions reveals folding principles of the human genome. 326, 289–293.
- Lin, D.C.-H., and Grossman, A.D. (1998). Identification and Characterization of a Bacterial Chromosome Partitioning Site. *Cell* 92, 675–685.
- Lin, Z., Deng, B., Jiao, Z., Wu, B., Xu, X., Yu, D., and Li, W. (2013). A versatile mini-mazF-cassette for marker-free targeted genetic modification in *Bacillus subtilis*. *J. Microbiol. Methods* 95, 207–214.
- McKinney, S. a, Murphy, C.S., Hazelwood, K.L., Davidson, M.W., and Looger, L.L. (2009). A bright and photostable photoconvertible fluorescent protein. *Nat. Methods* 6, 131–133.
- Murray, H., and Errington, J. (2008). Dynamic control of the DNA replication initiation protein DnaA by Soj/ParA. *Cell* 135, 74–84.
- Murray, H., Ferreira, H., and Errington, J. (2006). The bacterial chromosome segregation protein Spo0J spreads along DNA from parS nucleation sites. *Mol. Microbiol.* 61, 1352–1361.

- Rasmussen S., Nielsen, H., and Hanne Jarmer (2009) The transcriptionally active regions in the genome of *Bacillus subtilis*, *Mol. Microbiol.* 73, 6, 1365-2958
- Real, G., Autret, S., Harry, E.J., Errington, J., and Henriques, A.O. (2005). Cell division protein DivIB influences the Spo0J/Soj system of chromosome segregation in *Bacillus subtilis*. *Mol. Microbiol.* 55, 349–367.
- Sambrook, J., Fritsch, E.F., and Maniatis, T. (1989). *Molecular Cloning: A Laboratory Manual*. Cold Spring Harbor laboratory press.
- Sergé, A., Bertaux, N., Rigneault, H., and Marguet, D. (2008). Dynamic multiple-target tracing to probe spatiotemporal cartography of cell membranes. *Nat. Methods* 5, 687–694.
- Sliusarenko, O., Heinritz, J., Emonet, T., and Jacobs-Wagner, C. (2011). High-throughput, subpixel precision analysis of bacterial morphogenesis and intracellular spatio-temporal dynamics. *Mol. Microbiol.* 80, 612–627.
- Smits, W.K., and Grossman, A.D. (2010). The transcriptional regulator Rok binds A+T-rich DNA and is involved in repression of a mobile genetic element in *Bacillus subtilis*. *PLoS Genet.* 6, e1001207.
- Steinmetz, M., and Richter, R. (1994). Plasmids designed to alter the antibiotic resistance expressed by insertion mutations in *Bacillus subtilis*, through in vivo recombination. *Gene* 142, 79–83.
- Su’etsugu, M., and Errington, J. (2011). The replicase sliding clamp dynamically accumulates behind progressing replication forks in *Bacillus subtilis* cells. *Mol. Cell* 41, 720–732.
- Sullivan, N.L., Marquis, K. a, and Rudner, D.Z. (2009). Recruitment of SMC by ParB-parS organizes the origin region and promotes efficient chromosome segregation. *Cell* 137, 697–707.
- Wang, X., Montero Llopis, P., and Rudner, D.Z. (2014a). *Bacillus subtilis* chromosome organization oscillates between two distinct patterns. *Proc. Natl. Acad. Sci. U.S.a.* 111, 12877–12882.
- Wolter, S., Löschberger, A., Holm, T., Aufmkolk, S., Dabauvalle, M.-C., van de Linde, S., and Sauer, M. (2012). rapidSTORM: accurate, fast open-source software for localization microscopy. *Nat. Methods* 9, 1040–1041.
- Youngman, P.J., Perkins, J.B., and Losick, R. (1983). Genetic transposition and insertional mutagenesis in *Bacillus subtilis* with *Streptococcus faecalis* transposon Tn917. *Proc. Natl. Acad. Sci. U. S. A.* 80, 2305–2309.